Brief overview

A systematic error in terms of underestimated plate thickness from impact-echo and combined impact-echo and surface wave measurements is studied in Paper I. A new approach for estimation of Poisson's ratio and a new approach for Lamb wave phase velocity imaging with 2D arrays are proposed in Paper II and Paper III, respectively. A theoretical study about ZGV modes and inhomogeneous plates is studied in Paper IV.

Appendix A

Paper I

O. Baggens and N. Ryden. 2015.
Systematic errors in Impact-Echo thickness estimation due to near field effects. NDT & E International, 69:16-27.
DOI: 10.1016/j.ndteint.2014.09.003.

NDT&E International 69 (2015) 16–27

Contents lists available at ScienceDirect

NDT&E International

journal homepage: www.elsevier.com/locate/ndteint

Systematic errors in Impact-Echo thickness estimation due to near field effects

Oskar Baggens *, Nils Ryden

Division of Engineering Geology, Lund University, PO Box 118, SE-22100, Lund, Sweden

ARTICLE INFO

Article history:
Received 10 April 2014
Received in revised form
10 September 2014
Accepted 14 September 2014
Available online 22 September 2014

Keywords:
Concrete
Impact-Echo
P-wave velocity
Thickness
Near field effect

ABSTRACT

Near field effects are found to create systematic errors, within the range of about 5–15%, in thickness estimations from Impact-Echo (IE) testing. This paper studies near field effects from a point source in a combined Multichannel Analysis of Surface Waves (MASW) and Impact-Echo analysis. The near field creates deviations in the measured velocity of the P-wave and the Rayleigh-wave, which lead to an underestimated thickness. This systematic error is identified in both a numerical and a real field case. The results are also compared with the conventional Impact-Echo method.

1. Introduction

In civil engineering, efficient non-destructive quality control plays an important role in the optimization of resources for manufacturing, maintenance, and safety. For concrete construction, the thickness of plate-like structures is a parameter of particular interest [1–3]. Several techniques have emerged for determining this thickness in a non-destructive manner [4]. The Impact-Echo (IE) method is one such technique which provides a straightforward estimation of the thickness of a structure with only one accessible side.

Early studies using the IE method report thickness estimation accuracies within 3% [5]. Although recent advances show promising results for implementing non-contact scanning measurements [6], studies with more significant deviations exist [1,7,2]. In these studies the thickness is underestimated in 18 of 19 locations with a mean error of 8%. In many IE thickness testing applications, e.g. nuclear reactor containment walls or load carrying structures in bridges, a verification with a drilled core sample is often not possible. Further studies, as this paper, which can clarify and highlight difficulties and potential error sources, about IE thickness testing are therefore valuable.

The conventional IE method uses two estimated parameters: the thickness resonance frequency f_r and the P-wave velocity V_P [8]. The thickness resonance is measured from the dynamic response to a transient impact. The P-wave velocity is either measured or assumed. The thickness h is subsequently determined using the empirical relation:

$$f_r = \frac{\beta V_P}{2h} \tag{1}$$

where β is an empirical correction factor that is usually assigned the value 0.96 for concrete. In fact, the exact value of f_r corresponds to the minimum frequency of the first symmetric Lamb mode (S1) dispersion curve [9]. The group velocity is zero at this specific point (S1-ZGV) [10]. The next thickness resonance is related to the second anti-symmetric Lamb mode (A2), which is also a zero-group velocity point (A2-ZGV).

To properly evaluate plate properties such as the thickness parameter, Lamb wave theory must be used. Lamb wave theory states that a laterally infinite isotropic plate is defined by three independent parameters: the shear wave speed V_S, Poisson's ratio ν, and thickness h. Consequently, the accuracy of this type of non-destructive evaluation of plates is solely dependent on these three variables. As a result, traditional IE methods are usually complemented with some sort of surface velocity measurement to most accurately determine the thickness [11]. However, if exact values of f_r and V_P are known, an exact value of the thickness can be obtained using Eq. (1) only if a correct value of β is assumed. An alternative method of increasing accuracy is to calibrate a velocity that satisfies Eq. (1) using an exact thickness measurement from a core sample. This approach is, however, not applicable in the case of plates with one-sided access if non-destructive testing is desired.

V_P is usually estimated from the time taken by the first arriving wave to travel between two points separated by a known distance. One major source of uncertainty of the first arrival velocity is the

* Corresponding author.
E-mail address: oskar.baggens@tg.lth.se (O. Baggens).

http://dx.doi.org/10.1016/j.ndteint.2014.09.003

identification of the correct first arrival time. This uncertainty is due to the small displacement magnitude of the surface normal component of the first arriving wave. A common procedure is to identify the first value above a certain threshold, and to assume that this wave corresponds to a pure P-wave. Another approach, which may improve the identification, is to study the trend of the measured signal [12]. The velocity of the P-wave may also vary through the thickness due to a material gradient resulting from the casting of a concrete slab, if larger aggregates concentrate near the bottom of the slab [1]. Gibson showed a systematic difference between the P-wave velocity measured along the surface and through the thickness [4]. A gradient with an increasing P-wave velocity with depth has been observed by [1,13–15]. Popovics et al. proposed an additional correction factor to compensate for the slower P-wave velocity along the surface [1].

An alternative approach that eliminates difficulties in identifying the first arrival is to calculate V_P from the Rayleigh wave velocity V_R, estimated by means of spectral analysis of surface waves (SASW) [16]. This approach requires an assumed value of ν. Poisson's ratio can, for example, be determined from the ratio between the frequencies of S1-ZGV and A2-ZGV [10] or the ratio between the S1-ZGV frequency and V_R [17]. The latter approach requires a known value of the thickness.

More recent approaches use a combination of a multichannel recording and a multichannel IE analysis [18,19,7]. The specific evaluation procedures differ slightly in their approaches. However, the main concept is to introduce additional information from surface wave analysis, for example, by estimating V_R. Since at least three parameters are accessible, it is possible to incorporate Lamb wave theory. Then, all three plate parameters (V_S, ν, h) can be determined simultaneously. Compared with the traditional IE method, these types of analyses are not affected by the uncertainty of assuming a correct value of β.

A possible source contributing to the uncertainty in f_r is the presence of multiple peaks in the frequency response spectrum [20]. The use of a time frequency analysis has been suggested to enhance the identification of the correct S1-ZGV frequency [21,22]. The use of multichannel recordings is another approach to facilitate the identification of the correct S1-ZGV frequency. Summation of the traces in close vicinity to the point source can be used to make the S1-ZGV frequency more pronounced [18]. A similar approach uses a quantity described as a multicross spectral density [23].

Although several improvements to the IE method have been proposed, a remaining systematic error may result in an underestimated thickness [1,7,2]. This underestimation can occur if the P-wave velocity is underestimated or if the S1-ZGV frequency is overestimated (Eq. (1)). Of these two parameters, a velocity representative of the complete through thickness seems to be the most difficult parameter to measure. Most proposed methods are based on a P-wave and/or Rayleigh wave velocity measurement along the surface. A possible source of underestimated velocities along the surface may be due to near field effects, which in this case are due to the cylindrical spreading of waves from a point source and the interference of different wave modes [24–28]. To the authors' knowledge, the near field effect has not been previously studied in this context of combined IE and velocity measurements.

This study adopts a combined Multichannel Analysis of Surface Waves (MASW) and IE method. In conformance with the IE method, this type of analysis also assumes that the P-wave velocity can be obtained by studying the first arrival wave. The combined MASW/IE method measures the P-wave velocity (V_P), the Rayleigh wave velocity (V_R), and the S1-ZGV frequency (f_{S1-ZGV}). These three parameters are used to estimate the plate parameters V_S, ν, and h. The systematic variations of the measured parameters V_P, V_R, and f_{S1-ZGV} due to near field effects are studied for a plate without a velocity gradient with depth. These types of variations, within a few thickness distances from the source, are not specific for the studied MASW/IE method; in fact, they are present in all evaluations related to surface wave analysis and/or IE analysis. The results are therefore general for many cases. Finally, the influence of the evaluated thickness is further explored with both a synthetic and an experimental field case. The results from the MASW/IE method are also compared with the results obtained using the conventional IE method.

2. Lamb waves

Only two different wave types can exist in an isotropic infinite body, the P-wave and the S-wave [29]. In a laterally infinite plate, an additional boundary condition requires the stress traction to be equal to zero at the surfaces. Thus, it is possible for guided waves or Lamb waves to exist. Lamb waves are created from combinations of P- and S-waves that satisfy the traction-free boundary condition. An infinite number of combinations which satisfy this boundary condition exist. They are, however, governed by the same equation, the so-called Lamb wave equation:

$$\frac{\tan(\beta h/2)}{\tan(\alpha h/2)} = -\left[\frac{4\alpha\beta k^2}{(k^2-\beta^2)^2}\right]^{\pm 1} \tag{2}$$

where

$$\alpha^2 = \frac{\omega^2}{V_P^2} - k^2$$

$$\beta^2 = \frac{\omega^2}{V_S^2} - k^2$$

The Lamb wave equation is based on an assumption of plane wave propagation, and enforces that only certain combinations of wave numbers k and frequencies ω are possible. This is the origin of the dispersive nature of Lamb waves. No simple analytical solutions of the equation exist, and instead, numerical methods must be used [29]. The Lamb wave theory forms the basis for linear elastic wave propagation in plates.

The dispersive nature of Lamb waves can be illustrated in many ways. One possibility is to present dispersion curves in the frequency–phase velocity domain. Fig. 1a shows a selection of the dispersion curves (Lamb modes A0, S0, A1, and S1) for a plate with $\nu = 0.2$. The axes are normalized with the thickness h and the shear wave speed V_S. The curves are thus only dependent on ν. The curves in Fig. 1a are valid for all plates with $\nu = 0.2$.

The dispersion curves contain important information about the plate characteristics. The Rayleigh wave velocity can, for example, be determined by tracking the convergence of the phase velocity for the A0 and the S0 modes. The S1-ZGV point, which is the point of the minimum frequency of the S1-mode, is another quantity which can be determined. As mentioned before in Section 1, this point corresponds to the thickness resonance f_r used in the traditional IE method (Eq. (1)).

An expanded view of the S1-ZGV points for different values of ν is shown in Fig. 1b. The variations of the locations for the S1-ZGV points are only affected by ν. This implies that the value of fh/V_S for the S1-ZGV point is constant for a fixed value of ν, and serves as the theoretical link between the empirical β factor used in the IE method and an analytical expression as a function of ν [9,17]. The constant value of fh/V_S provides a direct way of determining the plate thickness once V_S, ν, and f_{S1-ZGV} are known.

The constant value of fh/V_S also reveals how the estimated thickness is affected by uncertainties in the quantities V_S, ν, or f_{S1-ZGV} (Fig. 1b). An overestimation of f_{S1-ZGV} yields an

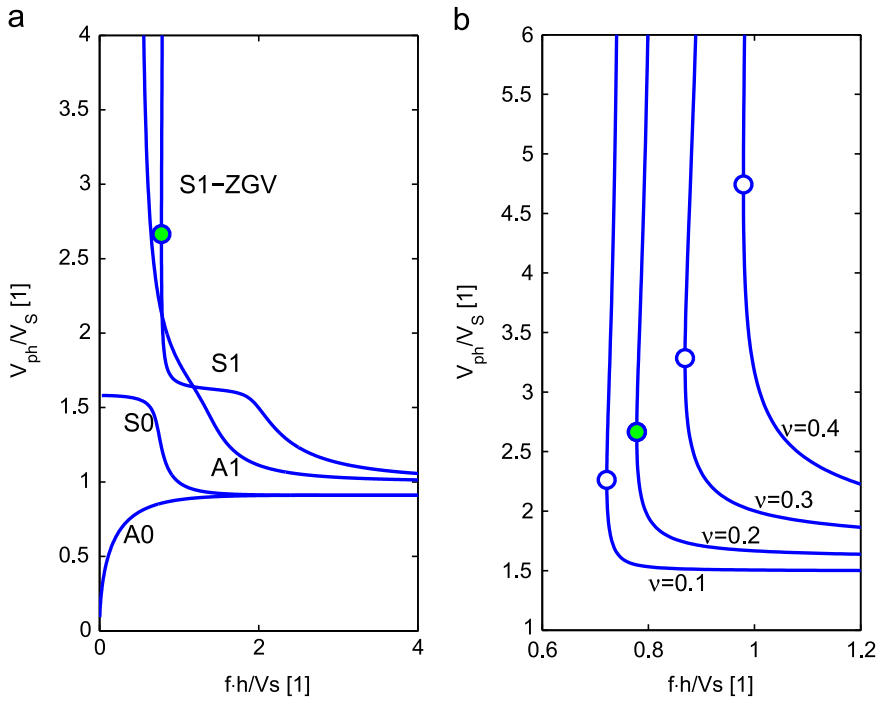

Fig. 1. (a) Lamb wave dispersion curves (A0, S0, A1, and S1 modes). (b) Expanded view around S1-ZGV points (S1 mode).

underestimated thickness, whereas an overestimation of V_S yields an overestimated thickness, assuming that the other two constants are exact. Finally, an overestimation of ν results in an overestimated thickness (Fig. 1b).

In practice, the plate parameters V_S, ν, and h are in most cases not directly accessible. Therefore, they must be determined indirectly using other parameters. One possibility is to measure V_P, V_R, and f_{S1-ZGV}, for example, by means of a combined MASW/IE method [18]. These three quantities provide the necessary information to determine V_S, ν, and h, and this approach was adopted in this study. The accuracy of the thickness estimation, which is of particular interest, is therefore dependent on the accuracy of the indirect parameters V_P, V_R, and f_{S1-ZGV}.

3. Numerical modeling

The presented theory in Section 2 assumes plane wave propagation, which at several wavelength's distance is a good approximation even for waves generated by a point source. As the radial distance of the studied waves decreases, this assumption becomes less valid, and near field effects are present. Furthermore, close to the source several different wave modes (e.g. P-waves, S-waves, Rayleigh waves) interfere with each other. A suitable approach for studying these two factors (i.e. near field effects) and the transition to the far field is to use a numerical model. A synthetic model, by means of Finite Elements (FE), was created in order to investigate the accuracy of the V_P, V_R, and f_{S1-ZGV} estimates determined by a combined MASW/IE technique. The model was created using commercial finite element software, Comsol Multiphysics [30]. A 2D axial symmetric plate was defined using a linear elastic material with Young's modulus of 36.1 MPa and a density of 2197 kg/m^3. The model was calculated using Poisson's ratios of 0.1, 0.2, 0.3, and 0.4, thus, covering a wide range of possible materials.

The thickness was set to 0.261 m and the length of the plate was 25 times longer than the thickness (Fig. 2). A short line load at the top surface was applied to simulate a point source. The load started at the symmetry axis and had a radius of 0.0025 m.

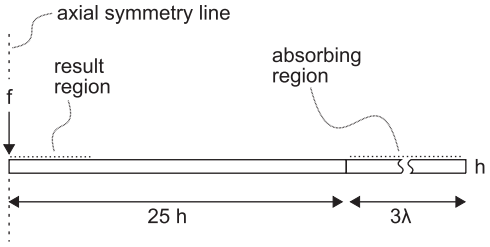

Fig. 2. FE-model sketch.

The plate was studied in the frequency domain, solving for the complex steady state response. A triangular element mesh with quadratic shape functions was used. A fine mesh with a minimum element length of 0.0025 m was used around the source location. In the rest of the model the element mesh was adjusted to have at least 10 elements per wavelength of the A0 mode. The mesh was thus adjusted for the solved frequencies using a coarse mesh for the low frequencies and a finer mesh for the high frequencies [31].

A silent boundary was created by a gradually increasing damping ratio in the absorbing region [32]. This region was added as an extension to the plate (Fig. 2). The length of the absorbing region was adjusted for the solved frequency with a length of 3 times the wavelength of the P-wave. The defined mesh and absorbing parameters were determined by a parametric convergence study of the theoretical Rayleigh wave velocity and S1-ZGV frequency.

In order to simulate the Impact-Echo and surface wave test, three synthetic force pulses were defined. The pulses were based on the Gaussian mono-pulse with different frequency contents (Fig. 3). The Gaussian mono-pulse was chosen to avoid energy at 0 Hz, as this energy can be difficult to handle in frequency domain simulations of a free plate. The pulses can be characterized as a low-frequency, mid-frequency, and high-frequency pulse with regard to the S1-ZGV frequencies (7–9 kHz) of the simulated plates.

The frequency domain responses along the upper surfaces of the plates from the pulses were calculated using the result from

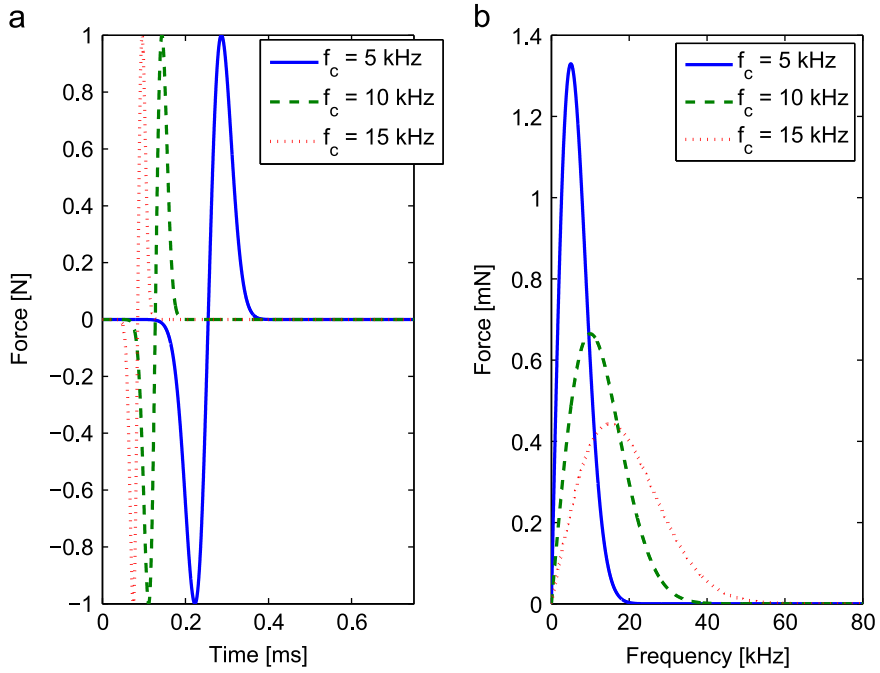

Fig. 3. Force pulses: (a) time domain, (b) frequency domain.

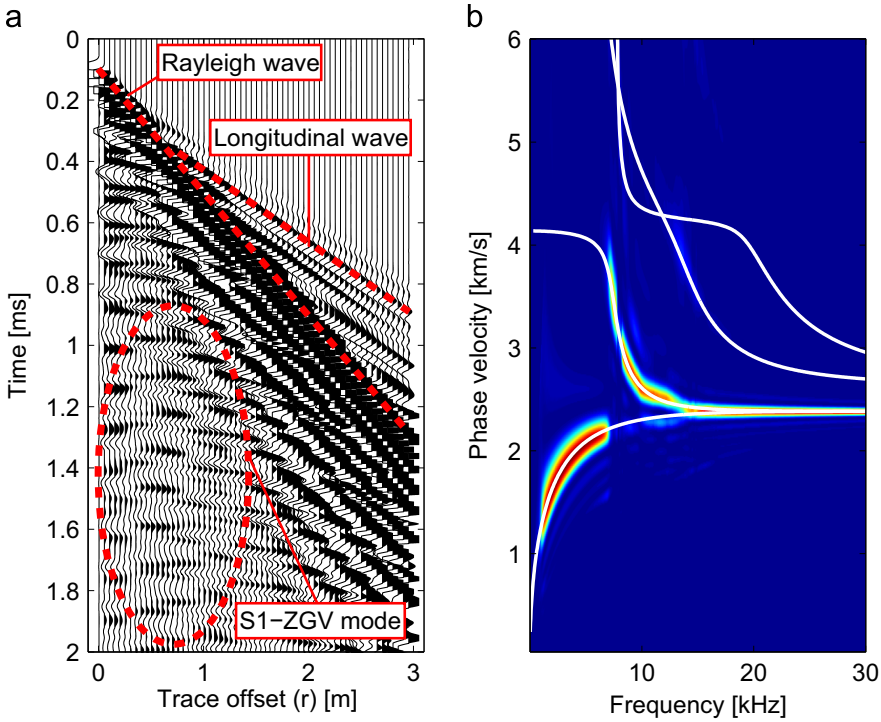

Fig. 4. Dataset: (a) time domain, (b) phase velocity–frequency domain.

the steady state analysis (Fig. 2). Subsequently, an inverse Fourier transform was performed to generate the response for the pulses in the time domain [32]. This concept was used to create synthetic multichannel datasets (Fig. 4a). The datasets were transformed into the phase velocity–frequency domain (Fig. 4b) [33]. It could be seen that the theoretical Lamb wave curves correlated well with the synthetic datasets. A detailed analysis of the difference between the simulated and theoretical values will be studied in the subsequent Results section.

4. Results

Estimates of the first arrival P-wave velocity (V_P), the Rayleigh wave velocity (V_R), and the S1-ZGV frequency (f_{S1-ZGV}) have been studied as a function of distance from the source in order to quantify the influence of the near field. In all the presented result plots the distance from the source has been expressed as radius divided by thickness (r/h). This scale is used to emphasize that results are roughly applicable to any plate thickness although an

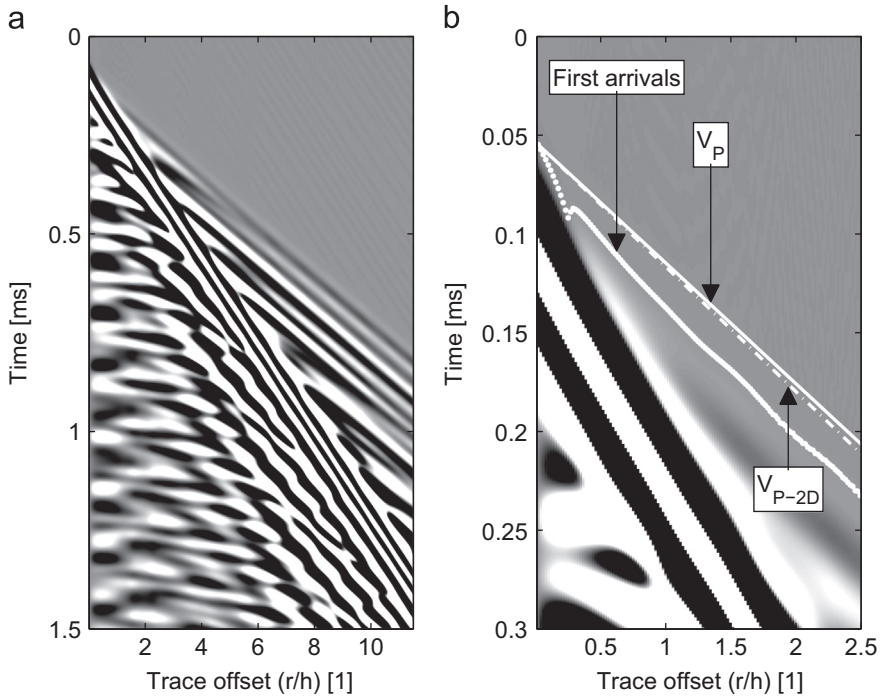

Fig. 5. Dataset $\nu=0.2$, $f_c=10$ kHz: (a) time domain, (b) expanded view, first arrivals.

exact normalization in both time (frequency) and space (wavelength) is not possible.

4.1. P-wave velocity

The variation of the first arrival P-wave velocity as a function of distance was studied for plate models with different values of ν. The models were studied in the time domain using the mid-frequency pulse (see Fig. 3). Fig. 5a shows the surface normal acceleration response to the mid-frequency pulse for the plate with $\nu=0.2$. The surface normal acceleration response was subsequently used to determine the first arrival P-wave.

Signals were gained in order to enhance the picture of the wave field and the first arrivals (Fig. 5b). In this type of commonly used seismic plot, the first arrival velocity close to the impact source appears to be close to the Rayleigh wave velocity. At a distance of about 1/4 of the thickness, there is a jump to a faster first arrival velocity which is closer to the P-wave velocity. The hidden first arrival of the P-wave is a consequence of the huge difference in amplitude of the Rayleigh wave and the P-wave (interference of modes).

First arrivals were picked for each trace at time points corresponding to the first absolute values above a threshold limit (Fig. 5b). The threshold limit was set at 10^{-4} of the maximum absolute value of the amplitude in each individual trace. Consequently, the threshold limit was reduced with an increasing radial distance. Fig. 5b also shows the theoretical first arrival P-wave velocity (V_P) along with the slightly slower quasi-P-wave velocity in plates (V_{P-2D}), marked with dotted lines. V_{P-2D} corresponds to the low frequency asymptotic value of the S0 Lamb mode in plates (Fig. 1a) and is the expected low frequency P-wave velocity in a plate [29]. The theoretical first arrivals were adjusted to intersect with the first arrival of the first trace.

The P-wave velocity was calculated by adjusting a slope to the first arrivals using linear regression. This evaluation was repeated while adding new traces to the array, and thus the length of the array was gradually extended. In all evaluations, the first trace was located at a fixed offset of 0.005 m from the impact center. This type of evaluation corresponds to a typical combined MASW/IE analysis.

In order to simulate the procedure used in the IE standard, the first arrival P-wave velocity was also calculated using two traces only. The first trace was selected at an offset of 0.005 from the impact center, and the second trace was selected at a distance of 0.3 from the first trace. The time difference of the first arrivals and the known distance of 0.3 m between the traces were used to yield the first arrival P-wave velocity. This calculation was repeated for different offset locations of the two traces, while maintaining a fixed internal distance between the traces of 0.3 m. This type of evaluation corresponds to the conventional Impact-Echo procedure when the first transducer is located at an offset of 0.15 m from the impact center [11].

The results from the MASW/IE and the IE type of analysis of the first arrivals are shown in Fig. 6a and b, respectively. The extracted velocities have been normalized with the theoretical P-wave velocity for each Poisson's ratio. In both types of analysis the initial normalized first arrival velocity close to the impact source is lower than the theoretical values. At a greater distance from the source, the normalized first arrival velocity gradually approaches the theoretical value. It can also be noticed that the sign of acceleration response (i.e., the direction) of the first arrivals is not constant and causes a discontinuity in the curve located at an offset of about 1/4 thickness. This shift of sign explains the momentarily high velocities of the IE type of analysis (Fig. 6b).

For Poisson's ratios 0.1 and 0.4, there are also other phase shifts at greater distances from the source. These phase shifts are caused by Lamb wave dispersion and generate extreme velocities in the IE analysis. Therefore, the first arrival P-wave velocity was only tracked until such an event occurred (Fig. 6b). The MASW/IE type of analysis is not affected in the same way, and it presents a more stable trend since it is based on an evaluation using multiple traces. It is also observed that the results for both evaluation methods are dependent on ν.

The above studied methods for determining the first arrival P-wave velocity are time domain evaluations, as are normally performed in practice. This type of analysis does not account for the dispersion which is typical for Lamb waves (Fig. 4b). Therefore, the dependency of frequency needed to be explored further.

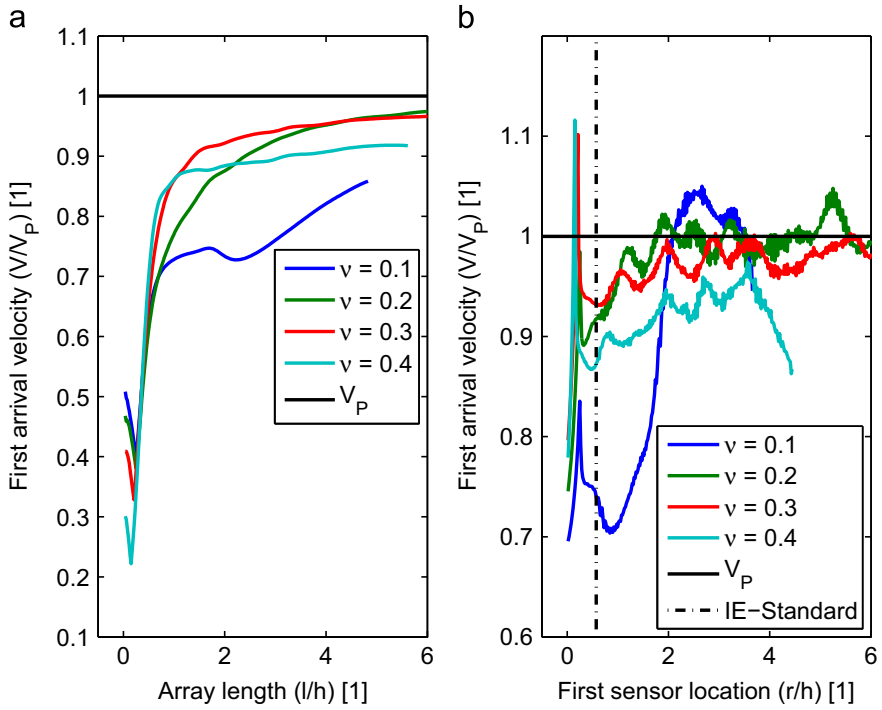

Fig. 6. First arrival velocity: (a) MASW/IE, (b) IE.

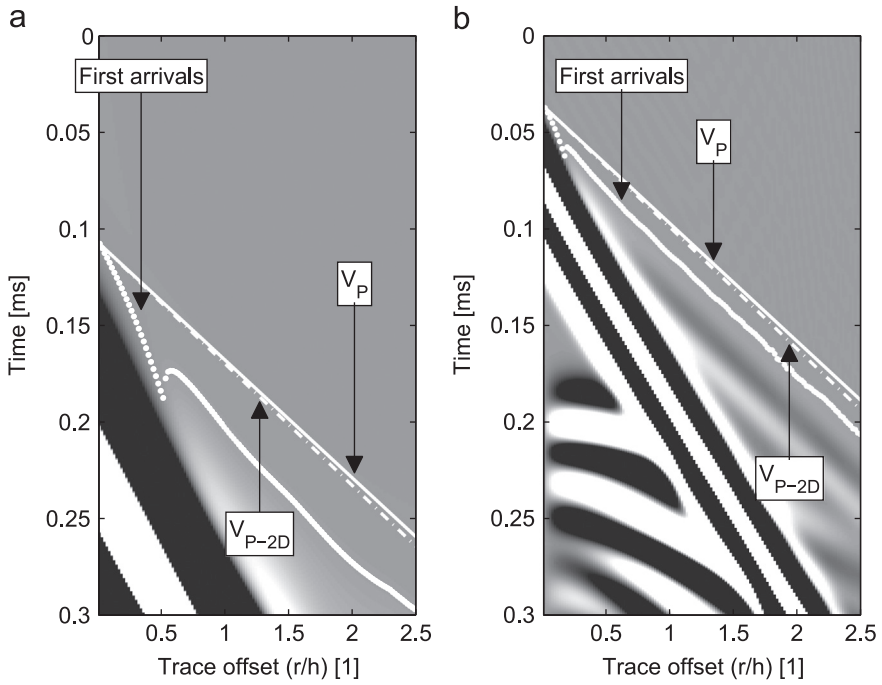

Fig. 7. Dataset, first arrivals: (a) $\nu=0.2$, $f_c=5$ kHz, (b) $\nu=0.2$, $f_c=15$ kHz.

The plate model with $\nu=0.2$ was chosen for a study using different pulses. The variation of the first arrival P-wave velocity as a function of distance was studied for the low, mid-, and high-frequency pulses. The surface normal acceleration responses of the low- and high-frequency pulses are shown in Fig. 7a and b, respectively.

It can be seen that the response of the low-frequency pulse (Fig. 7a) creates a larger zone with a slower first arrival velocity compared to that of the high-frequency pulse (Fig. 7b). This is consistent with the condition that a low-frequency pulse generates a response with a longer wavelength. The same type of evaluations for the first arrival P-wave velocity based on the MASW/IE and IE methods was performed for the different pulses. The results are shown in Fig. 8a and b. It can be noticed that variations in the estimated first arrival P-wave velocities are also dependent on the frequency content of the exciting pulses.

4.2. Rayleigh wave velocity, S1-ZGV frequency

The variation in V_R was studied for the plates with different values of ν. The mid-frequency pulse was used to create the

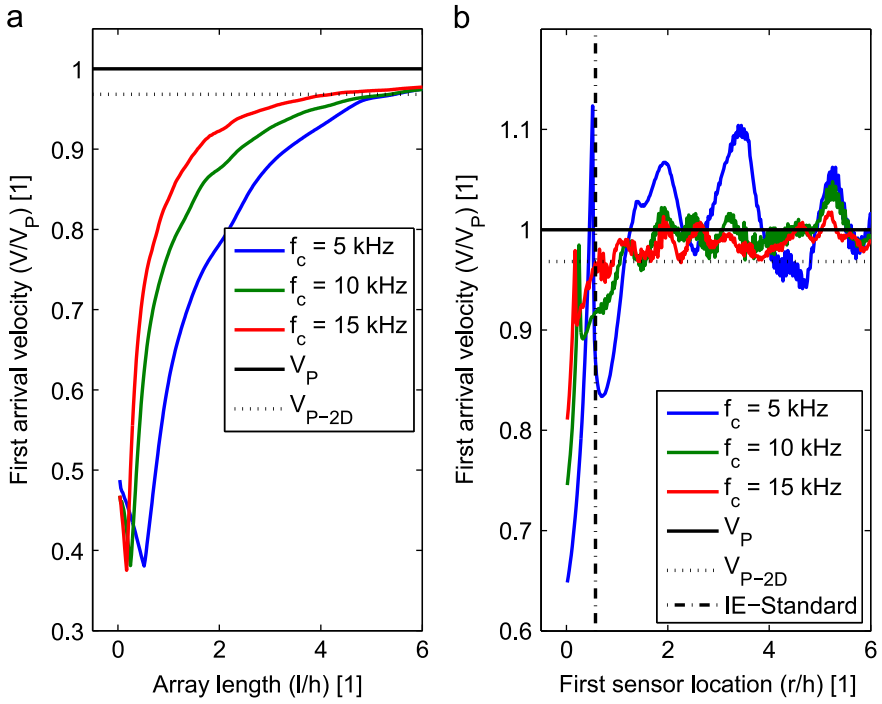

Fig. 8. First arrival velocity: (a) MASW/IE, (b) IE.

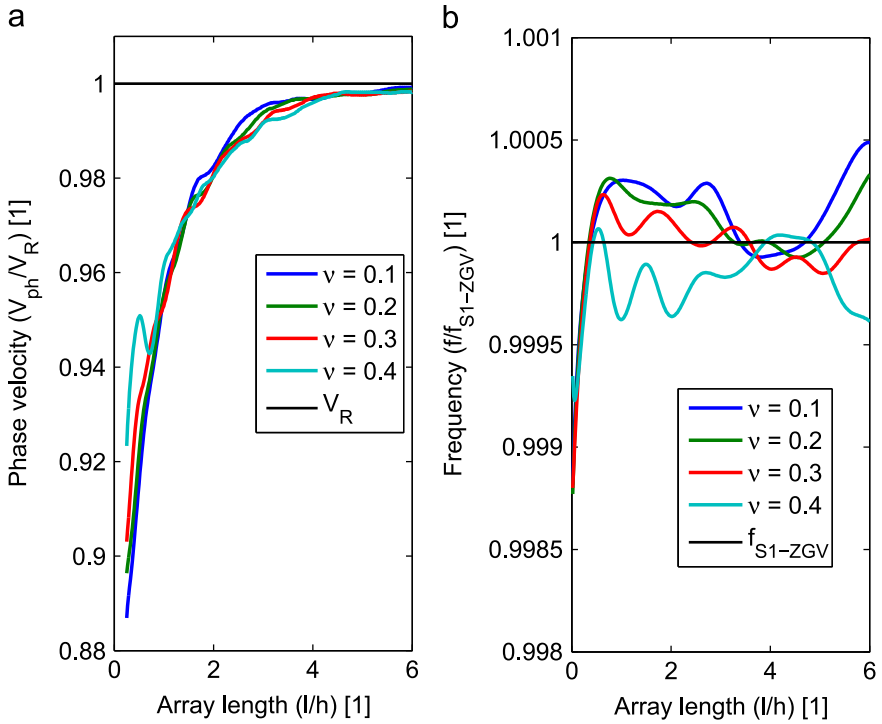

Fig. 9. (a) Rayleigh-wave velocity. (b) S1-ZGV frequency.

datasets. V_R was estimated by tracking the convergence of the A0 and S0 modes of the datasets in the frequency–phase velocity domain. This evaluation was made for different array lengths. The array was extended by adding new traces as with the study of the first arrival P-wave velocity. The extracted velocity is shown in Fig. 9a. It can be observed that V_R is underestimated close to the source, i.e. when the array in the combined MASW/IE method is short. Thereafter, the estimated velocity gradually increases and converges with the theoretical velocity when the array lengthens. The estimated velocity is dependent on ν. However, the main behavior is generally the same for all values of ν. The observed phenomena are in agreement with the results obtained by [26,28] for V_R in a half space. Roesset [26] showed analytically how the phase velocity for the response at the surface increases with the distance from the source in the case of a homogeneous half-space. This slower phase velocity close to the source is related to the variation in the interference between the bulk wave modes. For the studied case shown in Fig. 9a, the near-field effect is likely to

be even more complicated, since the geometry is a plate instead of a half-space. Furthermore, the use of an array as well as the frequency content of the impulse may also add additional complexity to the problem. Therefore, the result shown in Fig. 9a should not be interpreted exactly quantitatively but rather as a general trend partly explaining the observed underestimated thickness.

The S1-ZGV frequency was estimated using an offset summation technique [18]. This technique was used in the combined MASW/IE analysis to enhance the S1-ZGV resonance frequency peak [7]. The evaluation was made for different array lengths in the same manner as with the evaluation of V_R. The results from the S1-ZGV frequency estimations are shown in Fig. 9b. These estimations do not provide a completely constant value; instead, they oscillate slightly. These minor variations were assumed to be associated with uncertainties inherited from the nature of numerical modelling and evaluations. However, in comparison with the estimations of V_P and V_R, the estimations of f_{S1-ZGV} can be considered as accurate.

4.3. Thickness

The above demonstrated variations in the estimations of V_P and V_R indicate that a systematic error is present using the MASW/IE or the IE method. Thus, a systematic error is also present if the thickness is calculated from the estimations of V_P and V_R.

An estimate of the thickness as a function of distance was therefore calculated by combining the results in Figs. 6 and 9 from the mid-frequency source (f_c=10 kHz). These calculations were made using both the MASW/IE and IE techniques. In the MASW/IE analysis, ν was calculated from ratio of the first arrival P-wave velocity and the Rayleigh wave velocity. In this evaluation the first arrival P-wave velocity was assumed to correspond to the theoretical velocity of V_P. Thereafter, the thickness was calculated from the constant value of the quantity fh/V_S, as described in Section 2. The IE analysis used values of the first arrival P-wave velocity from Fig. 6b and a fixed value of the S1-ZGV frequency. This fixed value was extracted from the frequency spectrum of one single trace at a distance of 0.05 m from the source. The thickness was subsequently estimated using Eq. (1) with β=0.96 to mimic a real case evaluation where ν in general is not known beforehand. The estimated thicknesses by the MASW/IE and the IE method are shown in Fig. 10a and b, respectively.

For the MASW/IE analysis, ν was generally underestimated due to the underestimated ratio between the first arrival P-wave velocity and the Rayleigh wave velocity. Therefore, in the case of the model with a ν=0.1, it was not possible to estimate the thickness since the Lamb wave equation only was solved for values of ν from 0.10 to 0.45 (with increments of 0.01). This fixed increment of 0.01 explains the discontinuities in the curves in Fig. 10a. It can be observed that the MASW/IE type of method underestimates the thickness (Fig. 10a). As the estimates of V_P and V_R become more accurate, the estimated thickness subsequently becomes more accurate. Similar results were obtained from datasets with source frequencies f_c=5 kHz and f_c=15 kHz, although they are not plotted here. It should also be noticed that the alternative interpretation of the first arrival P-wave velocity as V_{P-2D} does not improve the results.

The estimated thickness from the IE method shows a more fluctuating result with a higher relative error compared to the MASW/IE analysis (Fig. 10b). The variation in the thickness (Fig. 10b) follows the variation of the estimated value of V_P (Fig. 6b), since the values for β and f_r were given a constant value when Eq. (1) was evaluated. It can be observed that the IE method for the case of this quite unrealistic value of ν=0.4 overestimates the thickness. This is due to the fixed value of β=0.96. A more suitable value would have been around 0.80 [9,17]. However, with real case data, the value of ν typically is not known beforehand. The analysis was therefore made with a fixed value of 0.96 for the β factor.

In the standard IE velocity measurement of the first arrival P-wave the estimated thickness is actually quite close to the true value (within 4%) after $r/h > 2$. With this set-up the problematic near field effect for a homogeneous plate is effectively minimized.

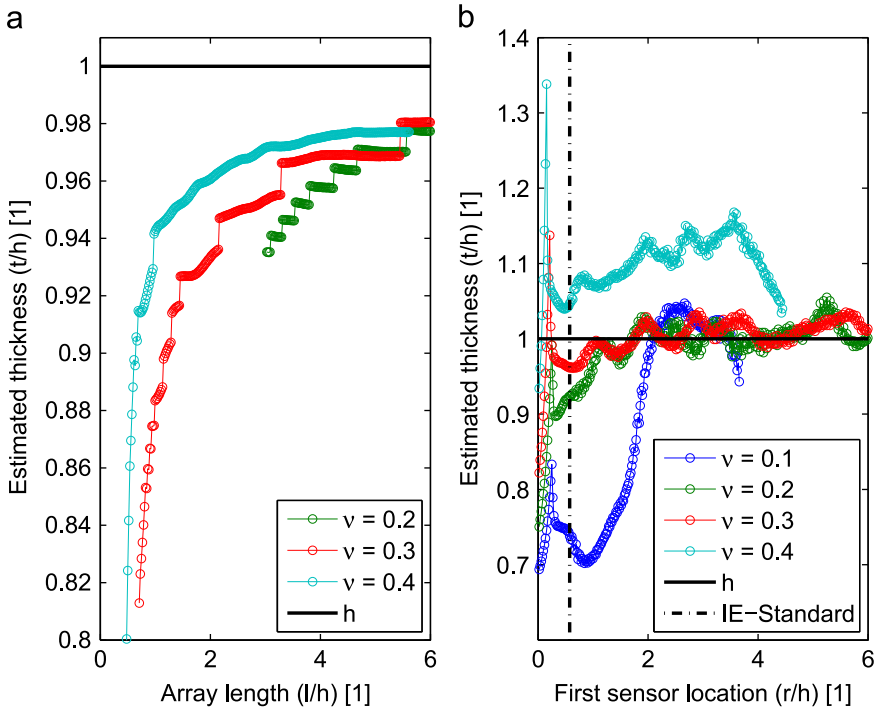

Fig. 10. Estimated thickness: (a) MASW/IE, (b) IE.

For the studied plate and source frequency this result is valid for all Poisson's ratios, except the quite unrealistic value of $\nu = 0.4$ for concrete.

5. Field case

The systematic error presented in Fig. 10 was further explored by studying a real field case. The aim of this field study was to investigate to which extent the near field effects could be observed in a real practical case. Field data was obtained from a Portland concrete cement plate cast on a granular base at The Advanced Transportation Research and Engineering Laboratory (ATREL), University of Illinois at Urbana-Champaign (UIUC). This plate is at the same location as location 5 in [7]. In this point the thickness was underestimated with all tested seismic techniques (4–13%).

Time-synchronized multichannel data were obtained using one accelerometer and a hammer with a trigger connected to a DAQ computer [34]. The accelerometer measured the surface normal component of the acceleration response. Data were collected over a distance of 1 m with an interval distance of 0.02 m between each hammer impact. The data could therefore be used for a MASW/IE and an IE analysis using the same evaluation techniques previously described. A core sample was also extracted from the center of the 1 m long MASW/IE array. The thickness was measured to 0.337 m [7].

A plot of the data in time domain and frequency–phase velocity domain can be seen in Fig. 11a and b, respectively. The locations of the first arrivals are marked with black dots in Fig. 11a. The first arrivals were identified at time points corresponding to the first absolute value exceeding a threshold limit. This threshold limit was set at 2.5×10^{-3} of the maximum absolute value in each individual trace. As in the synthetic case, the threshold limit was reduced with an increasing radial distance.

The indirect plate parameters V_P, V_R, and f_{S1-ZGV} were estimated in the same way as with the synthetic dataset. Estimations of the parameters were repeated using a different number of signals from the dataset, i.e., for different lengths of the measuring array. Thus, it was possible to create plots, similar to those previously presented, for the variation of the parameters with respect to the array length.

5.1. P-wave and Rayleigh wave velocity, S1-ZGV frequency

The variation of the first arrival P-wave velocity for the MASW/IE analysis can be seen in Fig. 12a. Fig. 12b shows the variation of the first arrival P-wave velocity using the IE type of measurement.

It can be observed that the first arrival P-wave velocity increases with the array length or the location of the sensors. This is the same general trend as with the synthetic case. The observed low resolution in Fig. 12b is a consequence of the low sample rate in the field data ($dt = 5$ μs) compared to the synthetic data case ($dt = 0.1$ μs). Ideally, a higher sample rate with lower value than $dt = 5$ μs should therefore be used.

It should be noted that a refracted P-wave can cause a similarly increasing velocity with distance due to an increasing stiffness within the concrete layer. In the analyzed test location, a velocity gradient (V_P=4450 m/s, 4765 m/s, 4828 m/s, from top to bottom) was actually observed by ultrasonic pulse velocity measurements of different sections of the extracted core sample. Assuming a top lower velocity layer with a thickness 0.05 m, a two-layer refraction model analysis can be made. From this, it is possible to estimate the radial distance for an appearance of a refracted P-wave [35]. It was found that a higher velocity from refraction could be predicted at a distance starting from about 1.5 thicknesses. Thus, it can be concluded that the material gradient cannot be the only explanation of the slower velocity close to the source in Fig. 12. Therefore, the consequence of the gradient in this case may act as an additional contribution to an increasing velocity with distance.

The estimations of the Rayleigh wave velocity and the S1-ZGV frequency are shown in Fig. 13a and b, respectively.

It can be seen in Fig. 13a that the Rayleigh wave velocity takes a lower value close to the source. Regarding the S1-ZGV frequency in Fig. 13b, a minor variation of the frequency is found. It was assumed that the S1-ZGV frequency also in this case could be

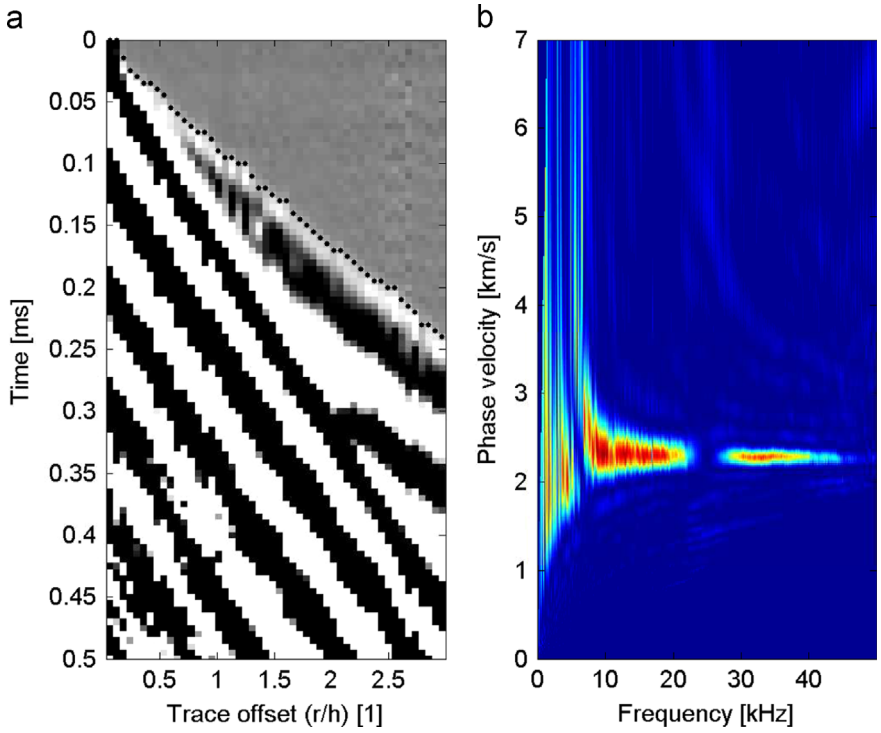

Fig. 11. Field data: (a) time domain, (b) phase velocity–frequency domain.

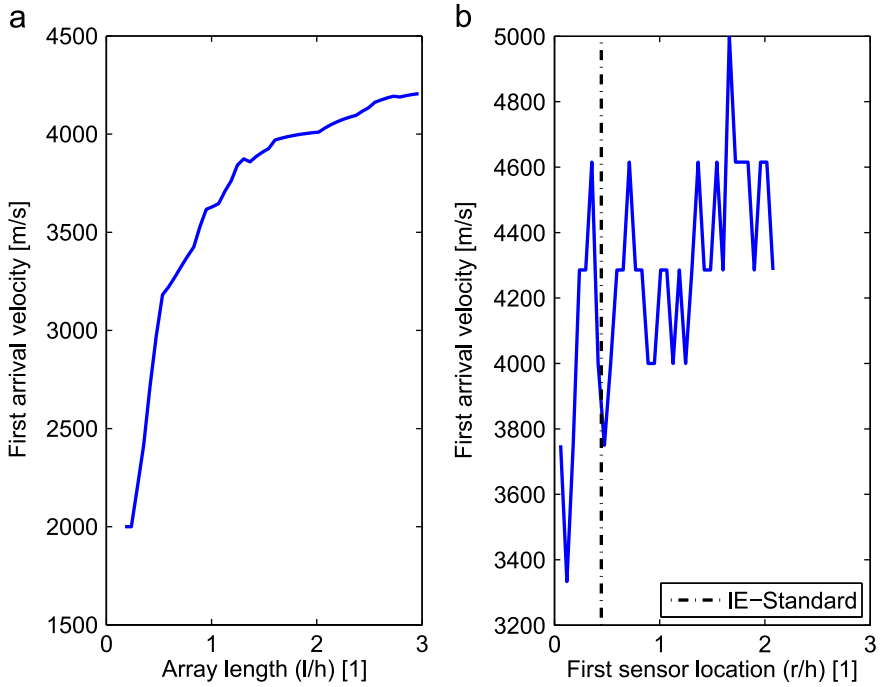

Fig. 12. First arrival velocity: (a) MASW/IE, (b) IE.

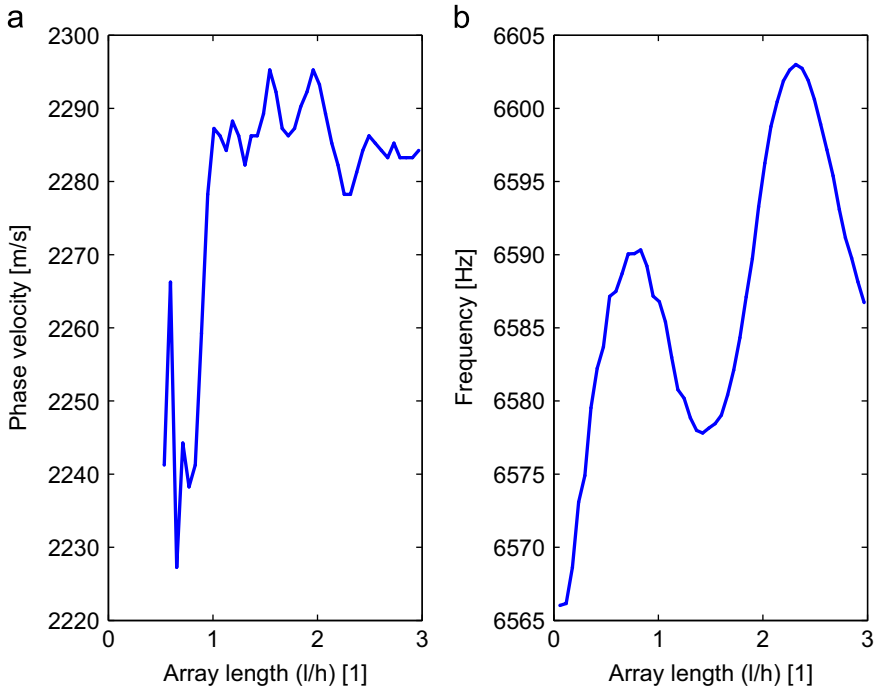

Fig. 13. (a) Rayleigh-wave velocity. (b) S1-ZGV frequency.

estimated with good accuracy. These observations for the Rayleigh wave velocity and S1-ZGV frequency are in agreement with the results obtained from the synthetic case.

Although the variations of the estimated parameters in Figs. 12 and 13 are not identical to the results from the synthetic dataset, it is possible to identify a common general behavior. It can also be observed that the estimated first arrival P-wave velocity shows the largest relative variation of the estimated quantities. The Rayleigh wave velocity shows the second largest relative variation, whereas the estimation of the S1-ZGV frequency only shows a minor relative variation. This result of the relative variation in the estimated parameters is in agreement with the result from the synthetic case.

5.2. Thickness

The estimations of V_P, V_R, and f_{S1-ZGV} were then subsequently used to calculate the variation in the corresponding estimated thickness. This calculation was made for the MASW/IE and IE types of methods, and followed the same procedure as for the synthetic case. The variation of the estimated thickness for the MASW/IE and IE types of methods can be seen in Fig. 14a and b, respectively.

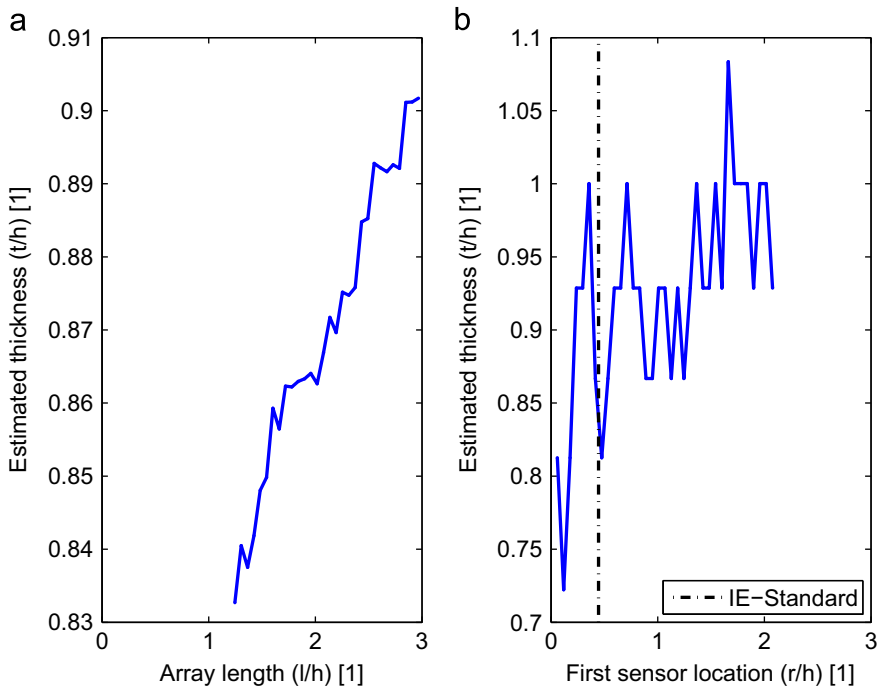

Fig. 14. Estimated thickness: (a) MASW/IE, (b) IE.

Fig. 14a shows that the MASW/IE analysis underestimates the thickness, especially when the array length is short. For the IE method in Fig. 14b, the thickness is underestimated in most cases. The IE method also shows a more fluctuating result due to the variation of V_P. It should be noted that part of this fluctuation originates from the relatively low sample rate. The general trend in Fig. 14 agrees qualitatively with the synthetic data presented in Fig. 10 within a distance of 3 thicknesses. It should be noted that longer array lengths are often unsuitable in practice and not desired since local plate properties are then smeared out. The observed larger underestimation in the field case, compared with the synthetic case, could be caused by the velocity gradient within the layer [1].

6. Conclusions

Numerical results show that near field effects can cause a systematic error in the estimation of thickness using a MASW/IE or a conventional IE method. The major source of error in the thickness estimations is related to the interpretation of the first arrival as a pure P-wave velocity. Detailed numerical analyses close to the point source reveal strong interference between the P-wave and the Rayleigh wave in the near field. This results in a zone where the first arrival velocity cannot be directly linked to the theoretical P-wave velocity. Furthermore, the size of this zone close to the point source is dependent on the plate properties and the source frequency content. This near field effect leads to an underestimated P-wave velocity from the picked first arrivals. These results further verify the inherently difficult and questionable task of estimating the P-wave velocity from first arrivals of dispersive Lamb waves.

The Rayleigh wave is also affected by the near field effect. Close to the point source, a lower value than the theoretical Rayleigh wave velocity is observed.

The S1-ZGV frequency is in general estimated with good accuracy.

The combined errors due to the near field effects create a systematic error which underestimates the thickness. This predicted systematic error of the estimated thickness from the MASW/IE and IE methods is found to be about 5–15% depending on Poisson's ratio, measurement set-up and source pulse. These findings are important for future improvements of non-destructive methods, such as the MASW/IE and IE methods.

Acknowledgments

Professor John S. Popovics is acknowledged for providing the experimental test site at The Advanced Transportation Research and Engineering Laboratory (ATREL), University of Illinois at Urbana-Champaign (UIUC) and for providing additional reference data of core samples. Professor Michael Lowe is acknowledged for valuable comments and discussions during the course of this study. The Development Fund of the Swedish Construction Industry (SBUF, No. 12534) and The Swedish Radiation Safety Authority (SSM, No. SSM2012-890) are acknowledged for financing the study.

References

[1] Popovics J, Cetrangolo G, Jackson N. Experimental investigation of impact-echo method for concrete slab thickness measurement. J Korean Soc Nondestruct Test 2006;26(6):427–39 URL ⟨http://www.dbpia.co.kr/Journal/ArticleDetail/3207698⟩.
[2] Maser KR. Non-destructive measurement of pavement layer thickness. Technical report. California Department of Transportation; 2003.
[3] Deacon JA, Monismith CL, Harvey JT. Pay factors for asphalt-concrete construction: effect of construction quality on agency costs. Technical report. Pavement Research Center, Institute of Transportation Studies, University of California, Berkeley; 1997.
[4] Gibson A. Advances in nondestructive testing of concrete pavements [Ph.d. thesis]. University of Illinois; 2004.
[5] Sansalone M, Streett W. Impact-echo: non-destructive evaluation of concrete and masonry. Jersey Shore: Bullbrier Press; 1997.
[6] Zhu J, Popovics JS. Imaging concrete structures using air-coupled impact-echo. J Eng Mech 2007;133(6):628–40. http://dx.doi.org/10.1061/(ASCE)0733-9399(2007)133:6(628) URL ⟨http://www.scopus.com/inward/record.url?eid=2-s2.0-34249020731&partnerID=tZOtx3y1⟩.
[7] Popovics J, Ryden N, Gibson A. New developments in NDE methods for pavements. Rev Quant Nondestruct Eval 2008;27:1320–7 URL ⟨http://scitation.aip.org/content/aip/proceeding/aipcp/10.1063/1.2902587⟩.

[8] Sansalone M. Impact-echo: the complete story. ACI Struct J 1997;94(6):777–86. http://dx.doi.org/10.14359/9737 URL ⟨http://www.concrete.org/Publications/ACIMaterialsJournal/ACIJournalSearch.aspx?m=details&ID=9737⟩.
[9] Gibson A, Popovics J. Lamb wave basis for impact-echo method analysis. J Eng Mech 2005;1–6. doi: http://dx.doi.org/10.1061/(ASCE)0733-9399(2005)131:4(438). URL ⟨http://ascelibrary.org/doi/abs/10.1061/(ASCE)0733-9399(2005)131:4(438)⟩.
[10] Clorennec D, Prada C, Royer D. Local and noncontact measurements of bulk acoustic wave velocities in thin isotropic plates and shells using zero group velocity Lamb modes. J Appl Phys 2007;101(3):034908. http://dx.doi.org/10.1063/1.2434824 URL ⟨http://link.aip.org/link/JAPIAU/v101/i3/p034908/s1&Agg=doi⟩.
[11] ASTM C 1383, Standard test method for measuring the P-wave speed and the thickness of concrete plates using the impact-echo method, annual book of American society for testing and materials (ASTM) standards.
[12] Popovics J, Song W, Achenbach JD, Lee JH, Andre RF. One-sided stress wave velocity measurement in concrete. J Eng Mech 1998;124(12):1346–53. http://dx.doi.org/10.1061/(ASCE)0733-9399(1998)124:12(1346) URL ⟨http://www.scopus.com/inward/record.url?eid=2-s2.0-0032455153&partnerID=tZOtx3y1http://ascelibrary.org/doi/abs/10.1061/(ASCE)0733-9399(1998)124:12(1346)⟩.
[13] Hu M, Lin Y, Cheng C. Method for determining internal P-wave speed and thickness of concrete plates. ACI Mater J 2006;103(5):327–35. http://dx.doi.org/10.14359/18154 URL ⟨http://www.concrete.org/Publications/ACIMaterialsJournal/ACIJournalSearch.aspx?m=details&ID=18154⟩.
[14] Qixian L, Bungey J. Using compression wave ultrasonic transducers to measure the velocity of surface waves and hence determine dynamic modulus of elasticity for concrete. Constr Build Mater 1996;10(4):237–42. http://dx.doi.org/10.1016/0950-0618(96)00003-7 URL ⟨http://www.sciencedirect.com/science/article/pii/0950061896000037⟩.
[15] Boyd A, Ferraro C. Effect of curing and deterioration on stress wave velocities in concrete. J Mater Civil Eng 2005;(April):153–158. doi:http://dx.doi.org/10.1061/(ASCE)0899-1561(2005)17:2(153). URL ⟨http://ascelibrary.org/doi/abs/10.1061/(ASCE)0899-1561(2005)17:2(153)⟩.
[16] Kim D, Seo W, Lee K. IE–SASW method for nondestructive evaluation of concrete structure. NDT & E Int 2006;39(2):143–54. http://dx.doi.org/10.1016/j.ndteint.2005.06.009 URL ⟨http://linkinghub.elsevier.com/retrieve/pii/S0963869505001003⟩.
[17] Medina R, Bayón A. Elastic constants of a plate from impact-echo resonance and Rayleigh wave velocity. J Sound Vib 2010;329(11):2114–26. http://dx.doi.org/10.1016/j.jsv.2009.12.026 URL ⟨http://linkinghub.elsevier.com/retrieve/pii/S0022460X0901027X⟩.
[18] Ryden N, Park C. A combined multichannel impact echo and surface wave analysis scheme for non-destructive thickness and stiffness evaluation of concrete slabs. In: AS NT, 2006 NDE conference on civil engineering; 2006. p. 247–53. URL ⟨http://scholar.google.com/scholar?hl=en&btnG=Search&q=intitle:A+Combined+Multichannel+Impact+Echo+and+Surface+Wave+Analysis+Scheme+for+Non-destructive+Thickness+and+Stiffness+Evaluation+of+Concrete+Slabs#0⟩.
[19] Barnes CL, Trottier J-F. Hybrid analysis of surface wavefield data from Portland cement and asphalt concrete plates. NDT & E Int 2009;42(2):106–12. http://dx.doi.org/10.1016/j.ndteint.2008.10.003 URL ⟨http://linkinghub.elsevier.com/retrieve/pii/S0963869508001217⟩.
[20] Schubert F, Wiggenhauser H, Lausch R. On the accuracy of thickness measurements in impact-echo testing of finite concrete specimens—numerical and experimental results. Ultrasonics 2004;42(1–9):897–901. http://dx.doi.org/10.1016/j.ultras.2004.01.076 URL ⟨http://www.ncbi.nlm.nih.gov/pubmed/15047403⟩.
[21] Abraham O, Leonard C, Cote P, Piwakowski B. Time frequency analysis of impact-echo signals: numerical modeling and experimental validation. ACI Mater J 2000;97:645–57. http://dx.doi.org/10.14359/9978 URL ⟨http://www.concrete.org/Publications/ACIMaterialsJournal/ACIJournalSearch.aspx?m=details&ID=9978⟩.
[22] Algernon D, Wiggenhauser H. Impact echo data analysis based on Hilbert–Huang transform. Transp Res Rec 2007;2028(1):146–53. http://dx.doi.org/10.3141/2028-16 URL ⟨http://www.scopus.com/inward/record.url?eid=2-s2.0-41549088922&partnerID=tZOtx3y1⟩.
[23] Medina R, Garrido M. Improving impact-echo method by using cross-spectral density. J Sound Vib 2007;304(3–5):769–78. http://dx.doi.org/10.1016/j.jsv.2007.03.019 URL ⟨http://linkinghub.elsevier.com/retrieve/pii/S0022460X07001824⟩.
[24] Zywicki D, Rix G. Mitigation of near-field effects for seismic surface wave velocity estimation with cylindrical beamformers. J Geotech Geoenviron Eng 2005;(August):970–977. doi:http://dx.doi.org/10.1061/(ASCE)1090-0241(2005)131:8(970). URL ⟨http://ascelibrary.org/doi/abs/10.1061/(ASCE)1090-0241(2005)131:8(970)⟩.
[25] Roesset J, Chang D, Stokoe K, Aouad M. Modulus and Thickness of the Pavement Surface Layer from SASW Tests. Transp Res Rec 1990;1260:53–63.
[26] Roesset J. Nondestructive dynamic testing of soils and pavements. Tamkang J Sci Eng 1998;1(2):61–80 URL ⟨http://www.researchgate.net/publication/237809455_Nondestructive_Dynamic_Testing_of_Soils_and_Pavements/file/72e7e52a9e73922ae7.pdf⟩.
[27] Ditri J, Pilarski A. Generation of guided waves in a plate by axisymmetric normal surface loading. In: Review of progress in quantitative nondestructive evaluation, vol. 13. URL ⟨http://books.google.com/books?hl=en&lr=&id=RWulSz94GPAC&oi=fnd&pg=PA133&dq=Generation+of+Guided+waves+in+a+plate+by+axisymnetric+normal+surface+loading&ots=CsnCME1_0P&sig=_5TG40-ePmiFOh187QJ4o5t5WBw⟩.
[28] Bodet L, Abraham O, Clorennec D. Near-offset effects on Rayleigh-wave dispersion measurements: physical modeling. J Appl Geophys 2009;68(1):95–103. http://dx.doi.org/10.1016/j.jappgeo.2009.02.012 URL ⟨http://www.scopus.com/inward/record.url?eid=2-s2.0-67349207134&partnerID=tZOtx3y1⟩.
[29] Achenbach JD. Wave propagation in elastic solids. Amsterdam, London: North-Holland Publishing Company; 1973.
[30] Comsol Inc, Comsol Multiphysics, 2014. URL ⟨http://www.comsol.com⟩.
[31] Ryden N, Castaings M, Thompson DO, Chimenti DE. An adaptive frequency domain finite element model for surface wave testing of pavements. AIP Conf Proc 2009;1096:1481–8. doi:http://dx.doi.org/10.1063/1.3114132. URL ⟨http://link.aip.org/link/APCPCS/v1096/i1/p1481/s1&Agg=doi⟩.
[32] Castaings M, Bacon C, Hosten B, Predoi MV. Finite element predictions for the dynamic response of thermo-viscoelastic material structures. J Acoust Soc Am 2004;115(3):1125. http://dx.doi.org/10.1121/1.1639332 URL ⟨http://www.scopus.com/inward/record.url?eid=2-s2.0-1542376817&partnerID=tZOtx3y1⟩.
[33] Park CB, Miller RD, Xia J. Multichannel analysis of surface waves. Geophysics 1999;64(3):800–8. http://dx.doi.org/10.1190/1.1444590 URL ⟨http://library.seg.org/doi/abs/10.1190/1.1444590⟩.
[34] Ryden N, Park CB, Ulriksen P, Miller RD. Multimodal approach to seismic pavement testing. J Geotech Geoenviron Eng 2004;130(6):636–45. http://dx.doi.org/10.1061/(ASCE)1090-0241(2004)130:6(636) URL ⟨http://www.scopus.com/inward/record.url?eid=2-s2.0-2942608989&partnerID=tZOtx3y1⟩.
[35] Sheriff RE. Encyclopedic dictionary of exploration geophysics, geophysical references series, vol 1. Society of Exploration, Tulsa; 1991.

Appendix B

Paper II

O. Baggens and N. Ryden. 2015.
Poisson's ratio from polarization of acoustic zero-group velocity Lamb mode.
The Journal of the Acoustical Society of America, 138(1):EL88-EL92.
DOI: 10.1121/1.4923015.

Poisson's ratio from polarization of acoustic zero-group velocity Lamb mode

Oskar Baggens[a] **and Nils Ryden**
Division of Engineering Geology, Lund University, P.O. Box 118, SE-22100, Lund, Sweden
oskar.baggens@tg.lth.se, nils.ryden@tg.lth.se

Abstract: Poisson's ratio of an isotropic and free elastic plate is estimated from the polarization of the first symmetric acoustic zero-group velocity Lamb mode. This polarization is interpreted as the ratio of the absolute amplitudes of the surface normal and surface in-plane components of the acoustic mode. Results from the evaluation of simulated datasets indicate that the presented relation, which links the polarization and Poisson's ratio, can be extended to incorporate plates with material damping. Furthermore, the proposed application of the polarization is demonstrated in a practical field case, where an increased accuracy of estimated nominal thickness is obtained.

[JM]
Date Received: March 20, 2015 **Date Accepted:** June 7, 2015

1. Introduction

The fascinating properties of acoustic zero-group velocity (ZGV) Lamb modes[1,2] have been demonstrated to be useful in several applications, such as measurements of acoustic bulk wave velocities and Poisson's ratio,[3] thin-layer thickness,[4] hollow cylinders,[5] interfacial bond stiffness,[6] and possibly air-coupled measurements.[7] In this study, we present a novel application of the amplitude ratio of the surface normal and the surface in-plane components, and demonstrate how it can be used to estimate Poisson's ratio. This investigation was carried out from the perspective of non-destructive testing of concrete structures under one-sided access test conditions, but our observations are also valid for any material and structure for which Lamb wave theory is a representative assumption.

The evaluation of the dynamic response to a transient impact is a common technique for estimation of the thickness and/or mechanical properties of plate-like concrete structures. This type of acoustic measurement technique, often referred to as an impact-echo measurement,[8] employs the ZGV resonance frequency of the first symmetric (S1) Lamb mode.[9] To determine the thickness and/or mechanical properties, the frequency of the S1-ZGV mode must be complemented with two additional parameters, e.g., transverse wave speed and Poisson's ratio.[10] Combined impact-echo and surface wave measurements,[11] where Poisson's ratio typically is determined from the longitudinal wave and the Rayleigh wave velocity,[12] can be used to obtain these two additional parameters. However, systematic errors from near-field effects and velocity variation through the thickness can lead to an uncertain estimation of Poisson's ratio.[11]

Alternative approaches that do not depend on an estimation of the longitudinal wave velocity are therefore important for accurate estimation of Poisson's ratio. One alternative strategy is to use the ratio between the S1-ZGV frequency and the minimum frequency of the second anti-symmetric Lamb mode.[3] This approach has been demonstrated successfully for several thin homogenous metal plates,[3] but only a few measurements have been reported for concrete plates.[13]

To date, there is a lack of techniques that are independent of longitudinal wave velocity and that can accurately determine Poisson's ratio for concrete plates with only one accessible side. An interesting alternative is based on the polarization of Rayleigh waves.[14] Inspired by this idea of using polarization to estimate Poisson's ratio, here we propose and explore a new approach for estimating Poisson's ratio based on the polarization and shape of the S1-ZGV Lamb mode. An advantage of this new approach is that a through-thickness representative estimation of Poisson's ratio is obtained, since the S1-ZGV mode exists through the entire thickness of the plate.

This study is divided into three parts. We first present the theoretical foundation for this approach. We then verify the presented approach using a set of numerical simulations. Finally, we demonstrate the utility of this approach in a realistic field case.

[a]Author to whom correspondence should be addressed.

2. Amplitude polarization of Lamb mode

According to Lamb wave theory, which defines linear elastic wave propagation along isotropic infinite plates, the possible combinations of angular frequencies ω and lateral wave numbers k that can exist in a free plate with a height h is defined by[10]

$$\frac{\tan(\beta h/2)}{\tan(\alpha h/2)} = -\left[\frac{4\alpha\beta k^2}{(k^2-\beta^2)^2}\right]^{\pm 1}, \tag{1}$$

where

$$\alpha^2 = \omega^2/V_L^2 - k^2,$$
$$\beta^2 = \omega^2/V_T^2 - k^2.$$

V_L and V_T are the longitudinal and transversal wave velocities, respectively. The positive sign of the exponent on the right side of Eq. (1) defines symmetric modes, whereas the negative sign defines anti-symmetric modes. The wave number k can be used to determine the displacement field of the plate. The amplitude for the displacement at the free surface for the surface in-plane U and surface normal W directions are given by[10]

$$U = ck\left(\frac{1}{\tanh(qh/2)} - \frac{2qs}{k^2+s^2}\frac{1}{\tanh(sh/2)}\right), \tag{2}$$

$$W = -cq\left(1 - \frac{2k^2}{k^2+s^2}\right), \tag{3}$$

where c is an arbitrary multiplicative constant. The parameters q and s are calculated according to

$$q = \sqrt{k^2 - k_L^2}, \quad s = \sqrt{k^2 - k_T^2},$$

where k_L and k_T are the longitudinal and transversal wave number, respectively.

Equation (1) was used to find the frequencies ω and wave numbers k of the S1-ZGV points corresponding to each value of Poisson's ratio ν in the range 0.1 to 0.4, with increments of 0.01. Variations in $|U|$ and $|W|$ as a function of ν are shown in Fig. 1(a). The arbitrary constant c, in this case the scaling of the curves, is selected to yield an amplitude of 1 for $|W|$ at $\nu = 0.1$. Figure 1(b) displays the variation of the absolute ratio $|W/U|$ as a function of ν. This dimensionless quantity, which can be interpreted as the polarization of the S1-ZGV Lamb mode, is only dependent on ν, thus providing an opportunity to estimate ν if the polarization is measured. This relation is critical to the proposed approach.

3. Numerical modeling

The relation in Fig. 1(b) is calculated without including material damping. However, in many practical applications such as measurements of concrete structures, material damping is present; from a theoretical point of view, true ZGV Lamb modes are in these cases strictly not defined.[15] For this reason, practical measurements were simulated to investigate whether the polarization relation in Fig. 1(b) can be used to estimate ν even though material damping is present. For simplicity, we hereafter use the S1-ZGV abbreviation to refer to the first thickness resonance of the plate, although, as mentioned previously, no true ZGV modes are strictly defined for absorbing plates.

An axially symmetric finite-element model was created with unit values for the thickness $h = 1$ m, Young's modulus $E = 1$ Pa, and density $\rho = 1\,\text{kg/m}^3$. Note that the analysis results of the simulations are independent of the exact values of h, E, ρ. Poisson's ratio was varied from 0.1 to 0.4, with increments of 0.01, and the loss factor

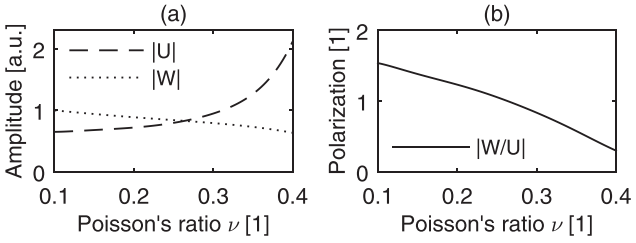

Fig. 1. (a) Absolute values of amplitudes components of S1-ZGV mode. (b) Polarization of S1-ZGV mode.

η was varied from 0 to 0.05, with increments of 0.01. A short line load starting at the axial symmetric axis and with a length of $0.02h$ was applied at the top surface to simulate an applied point load. Since the S1-ZGV frequency is dependent on ν, the center frequency of the load (Gaussian mono pulse) was set equal to the theoretical S1-ZGV frequency for the corresponding plate without material damping. The model was solved in the frequency domain using a frequency-dependent mesh and absorbing region.[16] The time domain response was obtained from the inverse discrete Fourier transform of the frequency domain response.

Synthetic datasets were created for all combinations of varying ν and η. Figure 2(a) contains the dataset for $\nu = 0.1$ and $\eta = 0.01$. In this plot, the normalized time history (y axis) of the surface in-plane acceleration response is shown for various normalized radial offset locations r/h (x axis) at the top accessible surface. Each dataset consisted of ten signals per length h within a radial distance of $4h$ from the axial symmetry axis. Similar to field measurements employing an impact point source, the broad frequency spectrum of the Gaussian mono pulse excites several Lamb modes. To reduce the influence from direct surface waves and enhance low group velocity modes (e.g., S1-ZGV), all signals were individually multiplied with a Tukey window. Figure 2(b) shows the amplitude of the window as function of time. The raw signals along with the windowed signals are shown in Fig. 2(a).

The mode shape at the S1-ZGV frequency was extracted using a temporal discrete Fourier transform of the windowed dataset. Figure 2(c) shows the absolute amplitude of the extracted mode at the S1-ZGV frequency for the surface in-plane and surface normal components as a function of the normalized radial distance r/h for the dataset with $\nu = 0.1$ and $\eta = 0.01$. Since the surface in-plane and surface normal components are not in phase, the polarization cannot be determined from two point-wise amplitudes at a fixed radial offset from Fig. 2(c) in a straightforward fashion. Instead, the spatial periodicity and amplitude for the total mode is used for simplicity and robustness. For straight crested Lamb waves, the spatial periodicity is defined by the exponential function. However, in this case, Hankel functions are used to account for cylindrical spreading from a point source.[17] Accordingly, the analytical expressions for the absolute amplitude of the S1-ZGV mode shape as function of amplitudes U, W, wave number k, and radial distance r take the form

$$A(U,k,r) = |\Re(|U|\mathrm{H}_1^{(1)}(kr)\mathrm{e}^{\mathrm{i}\arg(\mathrm{k})})|, \tag{4}$$

$$B(W,k,r) = |\Re(|W|\mathrm{H}_0^{(1)}(kr))|, \tag{5}$$

where A and B represent the surface in-plane and surface normal components, respectively. $H_1^{(1)}$ and $H_0^{(1)}$ are the first and zeroth-order Hankel functions of the first kind, respectively. We allow k to be complex-valued to account for material damping. The

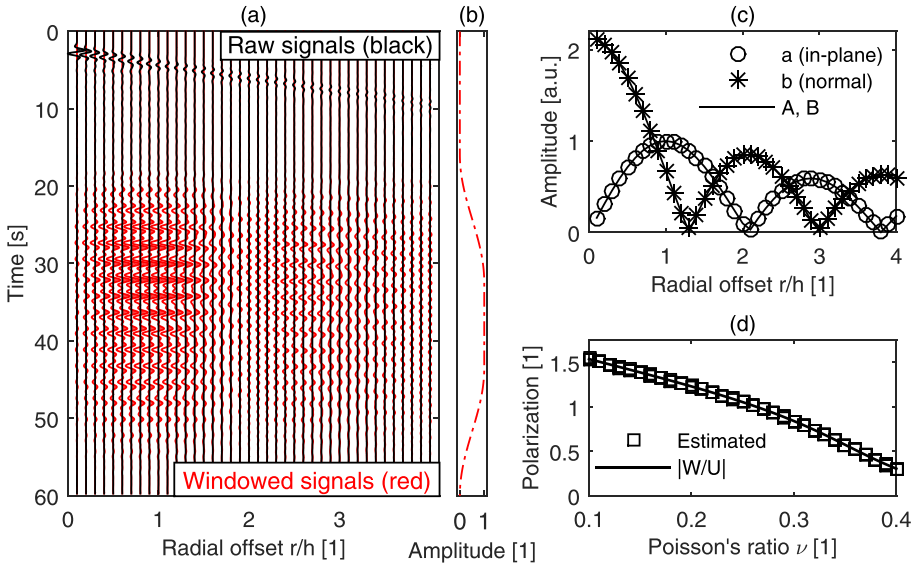

Fig. 2. (Color online) (a) Simulated multichannel dataset (surface in-plane component, $\nu = 0.1$, $\eta = 0.01$). (b) Tukey-window amplitude. (c) Absolute amplitude of extracted S1-ZGV mode (markers) and best solution (lines). (d) Estimated polarization (markers) and theoretical relation for lossless plates (solid line).

exponential term $e^{i\arg(k)}$ in Eq. (4) is introduced to maintain zero displacement at the axial symmetry axis ($r = 0$) when k is complex.

The absolute amplitudes $|U|$, $|W|$ and wave number k for the S1-ZGV mode of the simulated plate were estimated by searching for the best match between the analytic expressions in Eqs. (4) and (5) and the extracted mode shape [markers in Fig. 2(c)]. This search was carried out by minimizing the objective function

$$f(U, W, k, r) = \sum_{i=1}^{N} \left(\frac{(a_i - A_i)^2}{|U|} + \frac{(b_i - B_i)^2}{|W|} \right), \tag{6}$$

where a_i and b_i are the absolute amplitudes of the surface in-plane and surface normal components of the extracted mode, respectively [markers in Fig. 2(c)]. The index $i = 1, 2, \ldots, N$ labels the simulated signals, where $i = 1$ represents the signal nearest the impact point. A_i and B_i represents the functions from Eqs. (4) and (5) calculated at the radial offset $r = r_i$, i.e., $A_i = A(U, k, r = r_i)$ and $B_i = B(W, k, r = r_i)$. The function f was minimized by means of unconstrained nonlinear optimization using the *fmin-search* function available in MATLAB. Good agreement was obtained between the best solution to the minimization problem and the extracted mode [Fig. 2(c)]. The polarization was determined using $|W|$ and $|U|$ from this solution. This analysis, which enables the estimation of polarization, was repeated for each dataset (i.e., the simulated response to an impact pulse for the plate with varying combinations of ν and η). Figure 2(d) contains the estimated values of polarization for all datasets as well as the analytical relation [from Fig. 1(b)] calculated for lossless material. Good agreement exists between the analytical expression for the polarization and the simulated results. Note that the results from simulations that included material damping also match the analytical expression. Hence, the proposed approach is likely applicable to plates with material damping.

4. Field case

The proposed approach was tested on a concrete wall with a nominal thickness of 0.450 m. A three-component accelerometer attached to a fixed position on the wall was used to measure the response from hammer strokes performed at increasing offsets from the accelerometer. The input force from each stroke was also recorded. By using the reciprocity theorem for a linear elastic system, a multichannel dataset was obtained.[11] This dataset is of the same type as the simulated datasets in Sec. 3 and was processed in a similar way: a Tukey window was applied in the time domain, and then the absolute amplitude of the transfer function between the source and the receiver at the S1-ZGV frequency was extracted [Fig. 3(a)]. The objective function f from Eq. (6) was minimized using the same technique as in Sec. 3. Figure 3(a) illustrates the matched functions A and B.

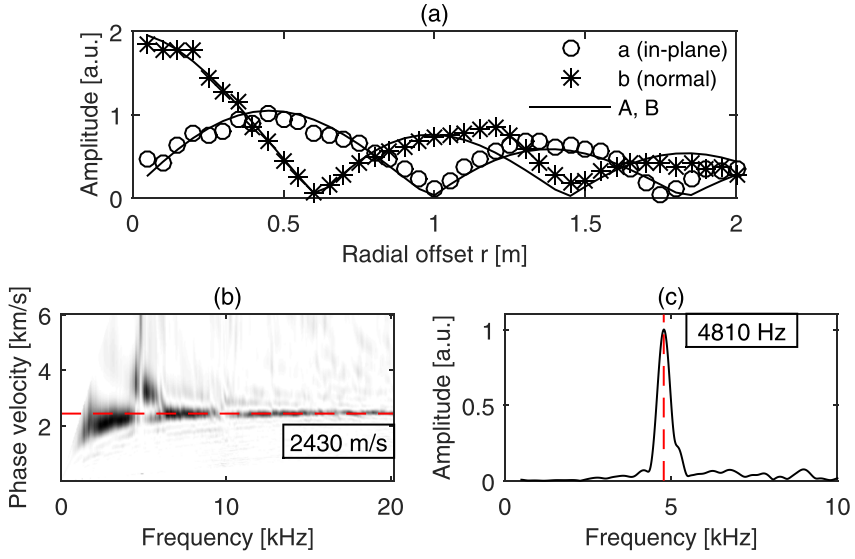

Fig. 3. (Color online) (a) Absolute amplitude of extracted S1-ZGV mode (markers) and best solution (lines). (b) Frequency-phase velocity spectrum, and estimated Rayleigh wave velocity (dashed line). (c) Frequency spectrum of (windowed) surface normal component signal nearest impact point (solid line), and estimated S1-ZGV frequency (dashed line).

The polarization $|W/U|$ was estimated as 1.09, yielding $\nu = 0.24$. Unfortunately, no exact value of ν is accessible for comparison. However, the estimation of ν can be verified indirectly to a certain extent from the nominal thickness of the wall $h = 0.450$ m. Estimation of the Rayleigh wave velocity (2430 m/s) from the raw signals displayed in frequency-phase velocity domain [Fig. 3(b)], the S1-ZGV frequency (4810 Hz) from the frequency spectrum of the windowed signal nearest the impact point [Fig. 3(c)], and Poisson's ratio (0.24) theoretically corresponds to a thickness of 0.447 m, which is within 1% error of the nominal thickness. The traditional approach[11] using the longitudinal wave velocity (4295 m/s) and Rayleigh wave velocity (2430 m/s), i.e., $\nu = 0.18$, theoretically corresponds to a thickness of 0.425, which is within 6% error of the nominal thickness. Thus, in this field case, our proposed approach provides a reasonable estimate of ν and an increased accuracy of the estimated nominal thickness, compared with the traditional approach.

5. Conclusions

Here we have presented a new approach to estimating Poisson's ratio from the amplitude polarization of the S1-ZGV Lamb mode. Numerical simulations demonstrated that this approach is also applicable to plates with material damping. A field-case example illustrated a benefit of this approach: a through-thickness representative value for Poisson's ratio is obtained via this strategy, thereby improving the overall estimation of plate parameters under one-sided access test conditions.

Acknowledgments

The Development Fund of the Swedish Construction Industry (SBUF, No. 12534) and The Swedish Radiation Safety Authority (SSM, No. SSM2012-890) are acknowledged for financing the study.

References and links

[1]E. Kausel, "Number and location of zero-group-velocity modes," J. Acoust. Soc. Am. **131**(5), 3601–3610 (2012).
[2]C. Prada, D. Clorennec, and D. Royer, "Local vibration of an elastic plate and zero-group velocity Lamb modes," J. Acoust. Soc. Am. **124**(1), 203–212 (2008).
[3]D. Clorennec, C. Prada, and D. Royer, "Local and noncontact measurements of bulk acoustic wave velocities in thin isotropic plates and shells using zero group velocity Lamb modes," J. Appl. Phys. **101**(3), 034908 (2007).
[4]M. Cès, D. Clorennec, D. Royer, and C. Prada, "Thin layer thickness measurements by zero group velocity Lamb mode resonances," Rev. Sci. Instrum. **82**(11), 114902 (2011).
[5]M. Cès, D. Royer, and C. Prada, "Characterization of mechanical properties of a hollow cylinder with zero group velocity Lamb modes," J. Acoust. Soc. Am. **132**(1), 180–185 (2012).
[6]S. Mezil, J. Laurent, D. Royer, and C. Prada, "Non contact probing of interfacial stiffnesses between two plates by zero-group velocity Lamb modes," Appl. Phys. Lett. **105**(2), 021605 (2014).
[7]S. D. Holland and D. E. Chimenti, "Air-coupled acoustic imaging with zero-group-velocity Lamb modes," Appl. Phys. Lett. **83**(13), 2704–2706 (2003).
[8]M. J. Sansalone and W. B. Streett, *Impact-Echo: Non-Destructive Evaluation of Concrete and Masonry* (Bullbrier Press, Jersey Shore, PA, 1997).
[9]A. Gibson and J. S. Popovics, "Lamb wave basis for impact-echo method analysis," J. Eng. Mech. **131**, 438–443 (2005).
[10]I. A. Viktorov, *Rayleigh and Lamb Waves Physical Theory and Applications* (Plenum Press, New York, 1967).
[11]O. Baggens and N. Ryden, "Systematic errors in Impact-Echo thickness estimation due to near field effects," NDT & E Int. **69**, 16–27 (2015).
[12]T. T. Wu, J. S. Fang, G. Y. Liu, and M. K. Kuo, "Determination of elastic constants of a concrete specimen using transient elastic waves," J. Acoust. Soc. Am. **98**(4), 2142–2148 (1995).
[13]A. Gibson, "Advances in nondestructive testing of concrete pavements," Ph.D. thesis, University of Illinois, Urbana-Champaign, 2004.
[14]A. Bayon, F. Gascon, and F. J. Nieves, "Estimation of dynamic elastic constants from the amplitude and velocity of Rayleigh waves," J. Acoust. Soc. Am. **117**(6), 3469–3477 (2005).
[15]F. Simonetti and M. J. S. Lowe, "On the meaning of Lamb mode nonpropagating branches," J. Acoust. Soc. Am. **118**(1), 186–192 (2005).
[16]M. Castaings, C. Bacon, B. Hosten, and M. V. Predoi, "Finite element predictions for the dynamic response of thermo-viscoelastic material structures," J. Acoust. Soc. Am. **115**(3), 1125–1133 (2004).
[17]J. J. Ditri, A. Pilarski, B. Pavlakovic, and J. L. Rose, "Generation of guided waves in a plate by axisymmetric normal surface loading," in *Review of Progress in Quantitative Nondestructive Evaluation* (Plenum Press, New York, 1994), Vol. 13A.

Appendix C

Paper III

O. Tofeldt and N. Ryden. 2017.
Lamb wave phase velocity imaging of concrete plates with 2D-arrays. Under review, Journal of Nondestructive Evaluation.

Lamb wave phase velocity imaging of concrete plates with 2D arrays

Oskar Tofeldt*, oskar.tofeldt@tg.lth.se, Tel. +46 (0)46 222 0000
Nils Ryden, nils.ryden@tg.lth.se

(Affiliation and address for both authors)
Division of Engineering Geology, Lund University
P.O. Box 118, SE-22100, Lund, Sweden

*Corresponding author

Abstract

In the nondestructive evaluation of concrete structures, ultrasonic techniques are considered to be more capable than low-frequency techniques such as the impact-echo method. This is especially true with the recent development of ultrasonic transducers, synthetic apertures, and results in an image form, and because low-frequency techniques are usually limited in their evaluation to the frequency of one single resonant mode. With the aim of reducing this gap in capabilities, we present a 2D array and wide-frequency bandwidth technique for Lamb wave phase velocity imaging. The presentation involves a measurement on a newly cast concrete plate using a hammer and an accelerometer as an example. The key concept of the technique is the use of 2D arrays that record a full wave field response over a limited surface subdomain within the complete measurement domain. Through a discrete Fourier transform, a spectral estimate is obtained for the 2D array in the frequency-phase velocity domain. The variation of the phase velocity is then mapped using a stepwise movement of the 2D array within the complete measurement domain. With two different types of 2D arrays, the variation of the phase velocity for the A0 Lamb mode is mapped and displayed in a polar and image plot, and low variation is observed for both cases. This result verifies the expected condition of a homogenous material and plate thickness and, more importantly, highlights the potential of wide-frequency bandwidth techniques based on full wave field data.

Keywords: Lamb waves; imaging; 2D arrays; concrete; impact-echo; full wave field data

1. Introduction

Nondestructive evaluation (NDE) techniques used on concrete structures can facilitate structural inspections, improve quality control, and support the sustainable use of resources [1]. Measurements based on vibrations and acoustic waves are frequently used to assess the mechanical properties in these structures. Such measurements are typically categorized based on their operating frequency, with ultrasonic methods as a major group. As a complement to the predominant use of ultrasonic reflection imaging approaches, we present a Lamb wave phase velocity imaging technique based on a full wave field response. Compared to ultrasonic approaches, this technique operates in a lower frequency regime and with a wider frequency content.

Ultrasonic testing allows the interior of a concrete construction element to be examined and visualized in the form of an reflection image [2, 3]. In this process, internal objects and anomalies such as defects appear as points or regions with deviating color. Techniques such as synthetic aperture focusing have made ultrasonic testing an effective, widely used, and powerful NDE approach for concrete structures. Recent progress has been made with this type of testing. One example is the development of wireless apertures that enable flexible data acquisition over larger areas compared to handheld devices [4]. However, for structures with heavy reinforcement or coarse aggregates, scattering and attenuation are challenges that may hinder the evaluation and reduce the ability to create a reflection image [3–6]. Since scattering and attenuation are related to the wavelength and number of cycles along the path of the ultrasonic pulse, this may particularly be a problem for high frequencies or thick structures [5].

To reduce the influence from scattering and attenuation, an alternative approach is to operate at a lower frequency regime, which leads to the usage of a longer spatial wavelength. This can, for instance, be achieved using a mechanical impactor as an input pulse source instead of an ultrasonic transducer. Based on this concept, the impact-echo (IE) method is a common and established technique for testing concrete structures [7]. In this method, an impact is applied to the surface using, for example, a hammer or a steel ball to generate a transient pulse with broadband frequency content. Ideally, the structural response to this transient excitation is dominated by a reverberating mode with a distinct frequency dependent on the material properties and geometry; i.e., the procedure corresponds to a general resonance test. Faults and anomalies can be detected by analyzing and monitoring the relative variation of the response along the surface. This procedure can be further extended with automatic data acquisition [8] and air-coupled sensors [9, 10] to generate a frequency image showing the relative variation of the response over a surface [8, 9].

There has been an improved understanding of the mechanism in IE testing over time. Whereas early studies interpreted the resonance mode as a discrete pulse with multiple reflections between the structural interfaces [7], more recent studies link the reverberating mode to the general theory of Lamb waves [11]. By showing that the resonance mode in IE testing corresponds to the first symmetric zero-group velocity (S1-ZGV) Lamb mode [11, 12], an important relationship to Lamb waves can be established. With this relationship determined at the outset and using the theoretical basis of Lamb wave theory, ongoing developments have advanced techniques that combine evaluation of the S1-ZGV Lamb mode frequency with propagating surface waves [13–17]. Such techniques, which use both propagating and nonpropagating modes with an analysis based on Lamb wave theory, enable a direct quantitative estimation of plate thickness and material velocity in absolute values; this differs from the original IE method that requires either a calibration sample or correction factor to provide the corresponding result [17]. In addition to quantitative estimations, the Lamb wave interpretation also facilitates the improved detectability and accuracy of the S1-ZGV frequency [18, 19] and enables an evaluation of Poisson's ratio [20] from the characteristics of the S1-ZGV Lamb mode shape.

Clearly, the results in the literature demonstrate the potential for using Lamb waves in the nondestructive evaluation of plate-like concrete structures. At present, these techniques are still mainly based on an evaluation at multiple discrete points [7, 8] or, in some cases, along line arrays with equidistant impact (signal) spacing [15]. Naturally, there is no prerequisite or limitation that only these two types of geometrical domains (point and line) can be used; other layouts have been observed in related applications such as geophysical investigations with surface waves [21] and Lamb wave testing of aluminum plates [22]. Thus, to improve the verification of the spatial distribution of results in the testing of plate-like concrete structures, a prospective methodology is to perform a

Lamb wave analysis with a two-dimensional (2D) surface considered in both the data collection and the data evaluation. To the authors' best knowledge, no examples of such an analysis with Lamb waves in the testing of plate-like concrete structures have been reported in the literature. This highlights the need for further investigations and serves as the motivation for the present study.

In this study, we demonstrate and describe a new technique for Lamb wave phase velocity imaging analysis of plate-like concrete structures. The technique is based on a full wave field dataset collected over a surface using an impact hammer and an accelerometer. In contrast to previous studies of concrete plates, which measured stationary modes at multiple discrete points over a surface, the novel aspect of this technique is that it evaluates propagating waves in multiple 2D subdomains (2D arrays). Flexibility in terms of operating frequency is obtained since the impact source creates a response with wide-frequency bandwidth. As a result, further developments of the presented technique have potential for the evaluation of large structures in which scattering and attenuation may present issues when using ultrasonic approaches.

The paper is organized as follows. In Section 2, we present a practical measurement as an illustrating example for the presented technique. Data processing and implementation of the technique are presented and explained in Section 3. First, data from a line array are processed in a conventional analysis of surface waves; this analysis is based on a 2D Fourier transform for which a discrete implementation is explained. Then, a transformation technique that converts data to a radial-offset domain is presented. The transformation allows the analysis of the data from the 2D arrays; as example, we analyze the phase velocity for the A0 Lamb mode and present the results in a polar and image plot. Finally, concluding remarks are provided in Section 4.

2. Method and measurement

We perform a measurement on a newly cast concrete slab that serves as the foundation and ground for a future school building. The entire slab (building) is approximately rectangular in shape with length 60 m and width 17 m. No joints appear within the extent of these outer boundaries; i.e., the slab is cast in a continuous assembly. The slab has a uniform nominal thickness of 0.12 m, except along the walls and bases of columns the thickness is increased to enhance the load-carrying capacity. More specifically, the measurement data in this study are acquired inside a rectangle with length 4 m and width 1.8 m. This rectangle is shown and highlighted in green in Fig. *1*(a). In turn, this rectangle is located in the center of a room with length 8.1 m and width 6 m, shown in Fig. *1*(a). The nominal thickness of the slab in the room follows the uniform standard value of 0.12 m, except along the top, left, and bottom edges of the room (gray color in Fig. *1*(a)) where the thickness is increased to 0.32 m to support the load from the inner walls. Along the right edge of the room, which also is at the edge of the slab (gold color in Fig. *1*(a)) and the outer wall, the nominal thickness is increased to 0.5 m. Except at this right edge of the room (slab edge), the distances to the outside edges of the slab are a minimum of 9 m. Thus, the location of the measurement ensures low influence from reflections caused by free slab edges. Moreover, since a newly cast plate is studied, it is expected that the slab will have uniform material properties and thickness and will be free of anomalies and defects. The measurement location is selected in order to create a controlled and reliable test environment that facilitates the development of new processing techniques without introducing excessive uncertainties.

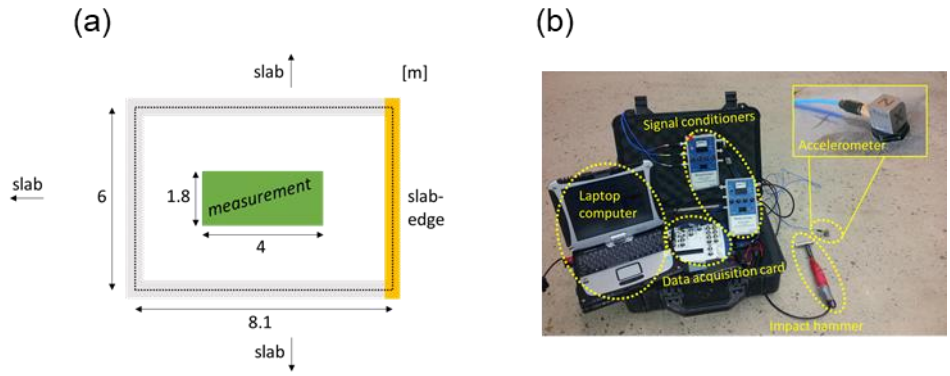

Fig. 1 (a) Sketch of measurement domain and (b) overview of measurement equipment

Measurement data are collected with portable equipment consisting of a three-component accelerometer (PCB model 356A15), impact hammer (PCB model 086C03), signal conditioners (PCB model 480b21), data acquisition card (NI USB-6251 BNC), and laptop computer. An overview of the equipment is shown in Fig. *1*(b). The collected data are composed of the vibration responses recorded by the accelerometer due to impacts made with the hammer. Responses from 1040 impacts are recorded at positions shown in Fig. *2*(a) as black dots. The accelerometer remains at a fixed position during the measurement, and it is marked with a red cross in the center of the measurement domain shown by the green rectangle in Fig. *2*(a) and (b). Fig. *2*(a) and (b) also show the orientation of the xyz-domain assigned to the measurement. For the direction parallel to the x-axis, the impact points appear at x-coordinates from +-0.05 m to +-2 m with offset intervals of 0.05 m between the points; note that no impact points appear along the line x = 0. For the direction parallel to the y-axis, impact points appear at y-coordinates from -0.9 m to +0.9 m with offset intervals of 0.15 m between the points. Fig. *2*(b) shows a photograph of the slab taken during the measurement. This figure depicts the rectangle (green color), the accelerometer (red cross), the coordinate system (yellow dotted lines), and the edge of the rectangular domain (yellow solid lines). For brevity, the 1040 impact points are not highlighted in Fig. *2*(b).

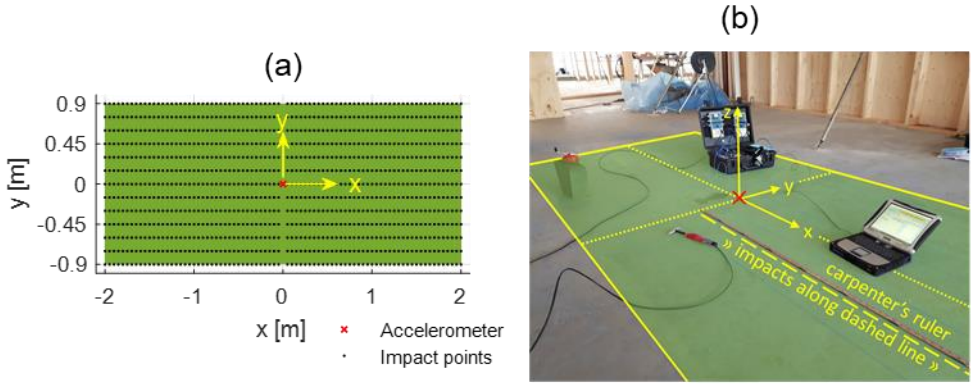

Fig. 2 (a) Measurement domain and associated coordinate system and (b) photograph from measurement with illustration of coordinate system and practical execution

Planning and organization are important in the collection of a large number of impact responses. In our case, we divide the 1040 points into 26 lines, each containing 40 impact points. Fig. *2*(b) shows an example of a line that is illustrated with yellow dashed markings. Along the line, 40 impacts are performed from left to right, covering a distance of $40 \cdot 0.05 = 2$ m. This corresponds to half of the rectangular domain length of 4 m. The 0.05 m offset distance between each point along the x-direction is maintained with guidance from the carpenter's ruler placed adjacent to the line; see Fig.

2(b). The process is then continued by marking a new line, for instance with a chalk line as used here, and thereafter collecting of a new set of 40 impacts. The described procedure is repeated 26 times in total, thus producing the 1040 impact points. Accordingly, it can be observed that the overall process corresponds to a series of measurements that are similar to those used in a multichannel analysis of surface waves (MASW) [23]. In the current measurement, each line requires approximately 5 minutes working time to mark the line and perform the impacts. Thus, 2–3 hours of effective working time are required to collect the complete dataset of 1040 impacts. It should be mentioned that a major part of this effective working time is spent on marking the appropriate location of the lines; typically, the impacts themselves are easily performed in a short amount of time.

For studies of vibrating systems, the coupling condition of the accelerometer is a crucial issue. In this study, the accelerometer is mounted with glue at the center of the rectangular domain (Fig. *2*(a) and (b), red cross) and it is kept in this position throughout the entire course of the measurement. This ensures a consistent coupling condition at the receiving end of the measurement system for all 1040 impacts, and it means that measurement uncertainty, except for electrical noise, is mainly generated at the sending end due to the potential variation in the coupling condition of the hammer impacts. In addition to generating the vibrations in the plate, the impact hammer also works as a triggering device; thus, reciprocity can be used. In more detail, reciprocity generally states that the response of a linear elastic system measured by an accelerometer at location A due to an impact applied at location B is equal to the response measured from the reciprocal arrangement, with the impact applied at location A and the accelerometer at location B. As a result, we are able to obtain a dataset containing the full wave field response from a transient point source excitation at the position of the accelerometer (Fig. *2*(a) and (b), red cross) recorded with 1040 sensors located at the impact points (Fig. *2*(a), black dots). In the following, this dataset is further studied and analyzed.

3. Data processing and results

The data acquisition card operates at the sampling frequency $f_s = 200$ kHz and a recording length of 20 ms, i.e., a recording length of 4000 samples. With the use of reciprocity, the collected dataset represents the full wave field response due to a point source excitation recorded with an array consisting of 1040 sensors. In the following, the aim is to demonstrate potential processing schemes relevant for this dataset by providing an explanation and details regarding the implementation of these schemes. The 1040 sensors are analyzed by dividing them into subsets of smaller groups. Accordingly, the groups can be interpreted as synthetic sensor arrays created by the geometrical shape that defines the group.

For this measurement, since a three-component accelerometer is used, each sensor records three individual signals: the acceleration response in the x-, y-, and z-directions. Thus, the dataset contains 3120 signals in total. In the following analysis, both the surface normal response (z-direction) and the surface in-plane responses (x- and y-directions) are considered. However, note that the presented analysis is not dependent on all components being measured; the adopted methodology is also applicable for data recorded with a conventional single-component accelerometer, which typically measures the surface normal component (z-direction).

3.1 Line array

An array defined by a line enables the study of a wave field in both space and time. In geophysical applications, this is often referred to as multichannel analysis of surface waves (MASW) [23], and similar approaches using this very general type of array are also used to test metal plates [24] and plate-like concrete structures [15]. Typically, for most applications, the arrays are characterized by uniform spatial sensor spacing along a line. In the case of this study, we create the array by selecting

sensors along the positive x-axis; see Fig. *3*(a) in which the blue diamond markers indicate the positions of the sensors and the red cross indicates the location of the transient point source excitation (from reciprocity). The array shown in Fig. *3*(a) consists of 40 sensors located every 0.05 m along the positive x-axis over the range $x = 0.05$ m to $x = 2$ m. For this line array case, we consider the signals containing the surface in-plane (x-direction) acceleration response and the surface normal (z-direction) acceleration response. Thus, the signals containing the acceleration response in the y-direction (transversal surface in-plane response) are ignored and not considered in the following analysis.

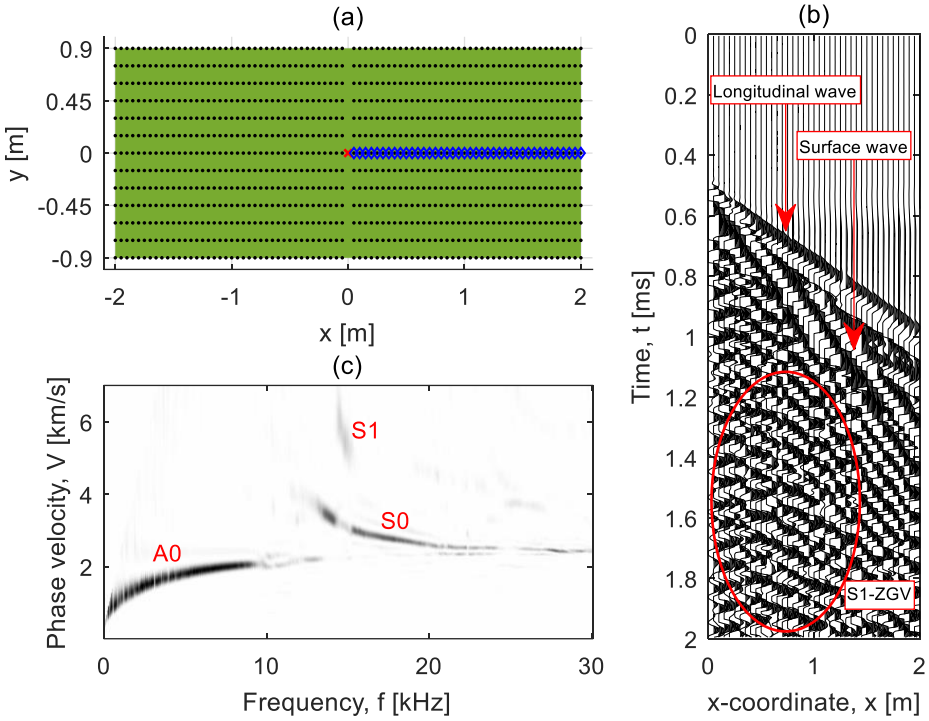

Fig. 3 (a) Measurement domain and line array shown with blue diamond markers, (b) time-domain low-pass filtered surface in-plane acceleration response and wave mode labels, (c) frequency-phase velocity correlation image and Lamb mode labels

Data corresponding to the surface in-plane (x-direction) acceleration response recorded with the array in Fig. *3*(a) are shown in Fig. *3*(b). For improved readability, the presented time domain data are low-pass filtered to reduce the frequency content above 30 kHz. Fig. *3*(b) shows the time history, up to 2 ms, of the signals that represent the surface in-plane acceleration response for all sensors in the array as a function of the x-coordinate of the sensors. This type of plot, sometimes referred to as a wiggle plot or seismic record, allows an initial analysis of the data in both time and space. In Fig. *3*(b), the longitudinal wave can be identified (see marking with arrow). After a time of approximately 1 ms, a stationary mode is observed. This mode corresponds to the S1-ZGV Lamb mode (see marking with ellipse), i.e., the reverberating mode typically analyzed in IE measurements of plates. Between the longitudinal wave and the S1-ZGV Lamb mode, a propagating surface wave can also be noticed (see marking with arrow).

Although the visualization of the data in Fig. *3*(b) possibly allows estimations of both velocity (slope in Fig. *3*(b)) and frequency (periodicity in Fig. *3*(b)), these estimations may be challenging since the recorded wave field consists of multimodal and dispersive Lamb waves that are present simultaneously over a wide frequency range. For this reason, estimations that are more robust are

generally obtained by transforming the data to the frequency domain in both time and space. This can be achieved using a 2D Fourier transform, as given by [25]:

$$S(k,f) = \int_{-\infty}^{+\infty} \int_{-\infty}^{+\infty} s(x,t)\, e^{-2\pi i(ft-kx)} dx\, dt \qquad \text{Eq. 1}$$

where S is the measured response as a function of spatial frequency (wave number) k and temporal frequency f, and s is the recorded vibration as a function of space x and time t. By using a discrete implementation (see Section X) of this transform and the relation $V = f/k$, where V is the phase velocity, the surface in-plane acceleration response is transformed to the frequency-phase velocity domain. The same transformation is also performed for the surface normal acceleration response. Then, a superposition of the transformed surface in-plane and surface normal responses is created and shown in Fig. *3*(c). Basically, Fig. *3*(c) shows the correlation for different combinations of frequencies f and phase velocities V for the data recorded by the array. The dark color indicates strong correlation, whereas the light color indicates weak correlation. In Fig. *3*(c), the two fundamental Lamb modes A0 and S0 can be identified (see markings). In addition, the part of the S1 Lamb mode curve related to the S1-ZGV Lamb mode can also be observed. This type of correlation image can be used to track the dispersive properties of the measured wave field. In other words, a Lamb wave dispersion analysis can be performed and used to evaluate the elastic properties and thickness of the plate [24]. Note that this type of analysis is independent of a priori information about the structure; compared with, for instance, the conventional IE technique [7], no empirical correction factors or calibration values are required [17].

3.2 Two-dimensional discrete Fourier transform

Since no analytical expressions exist for the measured response, the expression in Eq. 1 must be numerically evaluated to create the correlation image in Fig. *3*(c). The literature provides examples of implementing such evaluations [23, 25–29]. Although the format of implementation varies in the literature, the aim of estimating the spectral content in time and space is common. In this study, we adopt a discrete implementation described in a matrix format, since the matrix format is easily modified for arrays with nonuniform sensor spacing. Moreover, this format can be directly implemented in codes such as MATLAB. Here, the line array given by the blue diamond markers in Fig. *3*(a) is used as an illustrating example. However, it is emphasized that the implementation is general and applicable to other line arrays as well.

Let $\boldsymbol{s}[n]$ be a row vector containing the signal recorded by a sensor:

$$\boldsymbol{s}[n] = [s[1] \quad s[2] \quad \cdots \quad s[N]] \qquad \text{Eq. 2}$$

The index $n = 1, 2, \ldots N$ refers to each discrete sample of the signal in time. In this case, the vector $\boldsymbol{s}[n]$ contains $N = 4000$ discrete samples s recorded at time intervals $1/f_s$, where $f_s = 200$ kHz is the temporal sampling frequency. The spatial array consists of sensors that are numbered with index $m = 1, 2, \ldots M$. For the array studied here (blue diamond markers in Fig. *3*(a)), the number of sensors is $M = 40$. The sensors are located at the coordinates given by $x_m = m \cdot 0.05$, where 0.05 is the spatial sampling interval along the x-axis. The y-coordinates are for all sensors $y_m = 0$. An M-by-N matrix $\boldsymbol{S}$ containing the signals $\boldsymbol{s}_m$ for all sensors $m = 1, 2, \ldots M$ in the array is defined by

$$\boldsymbol{S} = \begin{bmatrix} \boldsymbol{s}_1 \\ \boldsymbol{s}_2 \\ \vdots \\ \boldsymbol{s}_M \end{bmatrix} \quad \text{Eq. 3}$$

In this case, the signal $\boldsymbol{s}_1$ corresponds to the sensor located closest to the point source location (red cross at $x = y = 0$ in Fig. *3*(a)), and $\boldsymbol{s}_M = \boldsymbol{s}_{40}$ corresponds to the sensor located farthest away from the point source. That is, the sensor signals in matrix $\boldsymbol{S}$ are sorted according to ascending distance from the point source according to ascending x-coordinates.

For the discrete Fourier transform in the time domain, a complex and discrete test function is defined by

$$\theta_f[n] = e^{-2\pi i\, f_{test}\, n/f_s} \quad \text{Eq. 4}$$

The test function θ_f describes a complex harmonic oscillation with frequency f_{test}. The subscript f indicates that the function is associated with frequency in the time domain. The term n/f_s can be interpreted as the time variable along which the function is periodic. By calculating the test function for $n = 1, 2, \ldots N$, i.e., for the same length and time as the signals $\boldsymbol{s}_m$, a test vector is created by

$$\boldsymbol{\theta}_f = \begin{bmatrix} \theta_f[1] \\ \theta_f[2] \\ \vdots \\ \theta_f[N] \end{bmatrix} \quad \text{Eq. 5}$$

Then, the discrete Fourier transform in the time domain is formulated as

$$\boldsymbol{s}_f = \boldsymbol{S}\boldsymbol{\theta}_f \quad \text{Eq. 6}$$

The resulting column vector $\boldsymbol{s}_f$ with length M contains complex numbers that are related to both the amplitude and phase of the spectral content for each sensor signal $\boldsymbol{s}_m$ at the test frequency f_{test}.

For the discrete Fourier transform in the space domain, a new complex and discrete test function is defined as

$$\theta_{f-V}[x_m] = e^{2\pi i\, f_{test}/V_{test}\, x_m} \quad \text{Eq. 7}$$

The test function θ_{f-V} describes a complex harmonic oscillation defined by the test frequency f_{test} and the test phase velocity V_{test}. The subscript $f - V$ indicates that the function is associated with frequency in time and the phase velocity. As a result, the function is defined by frequency in the space domain given by a test wave number $k_{test} = f_{test}/V_{test}$. This means that the function θ_{f-V} is periodic along the spatial x-axis of the array. The test function is calculated for the x-coordinates of each sensor to create a new test vector:

$$\boldsymbol{\theta}_{f-V} = \begin{bmatrix} \theta_{f-V}[x_1] \\ \theta_{f-V}[x_2] \\ \vdots \\ \theta_{f-V}[x_M] \end{bmatrix} \quad \text{Eq. 8}$$

The discrete Fourier transform in space domain is then given by

$$s_{f-V} = (\boldsymbol{s}_f \oslash \mathrm{abs}(\boldsymbol{s}_f))^{\boldsymbol{T}} \boldsymbol{\theta}_{f-V} \quad \text{Eq. 9}$$

where ⊘ is an element-wise division (Hadamard division) and $\mathrm{abs}(\boldsymbol{s}_f)$ is the absolute value of each element in the vector $\boldsymbol{s}_f$. Here, the element-wise division with the absolute values of the elements in $\boldsymbol{s}_f$ is used as a normalizing operation that removes the dependency on the amplitude of the wave field. Thus, this discrete Fourier transform in the space domain corresponds to an analysis of the phase angles of the complex elements in vector $\boldsymbol{s}_f$. This means that the magnitude of the resulting transformation given by s_{f-V} represents a measure of the correlation showing the extent to which a wave mode with frequency f_{test} and phase velocity V_{test} exists in the recorded wave field. The subscript $f-V$ is used to symbolize the association with both frequency f and phase velocity V. In the implementation presented here, s_{f-V} represents a complex scalar value. Thus, for the creation of a correlation image as presented in Fig. *3*(c), the above steps may be repeated over a range of combinations of test frequencies f_{test} and test phase velocities V_{test}.

In this example, the correlation image in Fig. *3*(c) is created by calculating s_{f-V} for both the surface in-plane (x-direction) and the surface normal (z-direction) responses. The transformed responses are then combined in the correlation image to $(|s_{f-V,\mathrm{in-plane}}|+|s_{f-V,\mathrm{normal}}|)^2$. The parenthesis is squared to facilitate the contrast of the correlation image, i.e., the power of the parenthesis acts as a modulating gain. Here, note that although the surface in-plane component and the surface normal component of Lamb modes in general are different in both phase and magnitude along the propagation axis, the frequency and phase velocity of a Lamb mode is the same for both components. For this example, an improved correlation image quality is obtained by the usage of two components instead of one component.

3.3 Radial offset domain transformation

By assuming cylindrical spreading of the wave field due to a point source, the processing scheme for a line array can be extended to include 2D arrays created by groups of sensors defined by a surface. Practically, this can be realized by transforming the recorded data to a radial offset domain. In the radial offset domain, the locations of the sensors are defined by a spatial radial coordinate r that measures the distance from the sensor to the source location (red cross in Fig. *2*(a) and (b)). Naturally, the radial coordinate r_m for a sensor m is given by

$$r_m = \sqrt{x_m^2 + y_m^2} \qquad \text{Eq. 10}$$

where x_m and y_m are the coordinates for the sensor m in the xy-plane. In other words, the radial offset domain represents a polar domain with a radial axis r directed outward from the center of the domain located at $x = y = 0$ (the location of the transient source from reciprocity).

In the radial offset domain, two acceleration responses are used: the surface normal response (z-direction) and the surface in-plane response (r-direction). Note that the z-axis in the radial offset domain is the same as the z-axis in the initial xyz-domain displayed in Fig. *2*. For this reason, no action is needed for the signals containing the surface normal response (z-direction); this response is only dependent on one physical channel of the accelerometer. However, to obtain the surface in-plane response (r-direction) in the radial offset domain, a simple transformation of the initially recorded data is required since this response is dependent on two physical channels (components) of the accelerometer. Accordingly, the surface in-plane acceleration response (r-direction) signal $\boldsymbol{s}_{m,in-plane}$ for a sensor m can be obtained by

$$\boldsymbol{s}_{m,in-plane} = (\boldsymbol{s}_{m,x} x_m + \boldsymbol{s}_{m,y} y_m)/r_m \qquad \text{Eq. 11}$$

where $\boldsymbol{s}_{m,x}$ and $\boldsymbol{s}_{m,y}$ are the signals containing the surface in-plane acceleration response in the x- and y-directions for the sensor m, respectively. That is, $\boldsymbol{s}_{m,in-plane}$ is obtained by projecting the acceleration response in the x- and y-direction onto the polar radial r-direction.

To proceed and further develop the study, the described transformation technique is applied to the collected dataset. An example of the output from this transformation is presented in Fig. 4, which shows the normalized surface in-plane (r-direction) acceleration response (Fig. 4(b)) and the normalized surface normal (z-direction) acceleration response (Fig. 4(c)) for the sensors marked with blue diamonds (Fig. 4(a)). For improved readability, the presented time-domain data are low-pass filtered to reduce the frequency content above 30 kHz. The selected sensors in Fig. 4(a) represent 14 sensors located at the radial offset distance $\mathrm{r} = 1.7 \pm 0.01$ m, i.e., at approximately the same radial offset distance r from the point source (red cross in Fig. 4(a)). In both Fig. 4(b) and (c), the signals from the 14 sensors show similar behavior. The consistency among the signals, showing the first arrival of the longitudinal wave around 0.9 ms and a surface wave around 1.2 ms, indicates that the plate under investigation is homogenous. Moreover, this consistency also implies a reliable and robust triggering in the time domain for each sensor. After around 1.7 ms, the signals are no longer consistent. This is related to the exposure of the sensors to different amounts of scattering and reflections; thus, we anticipate the reduced consistency as a function of time, as observed here.

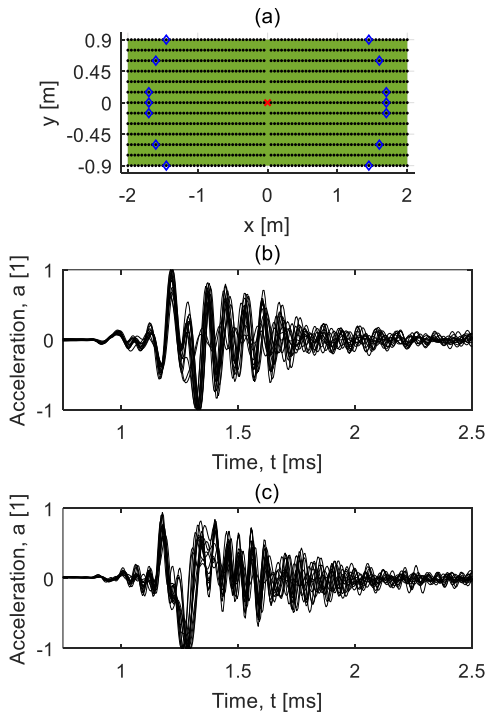

Fig. 4 (a) Measurement domain and sensors shown with blue diamonds, (b) corresponding time-domain low-pass filtered acceleration response for surface in-plane direction and (c) surface normal direction

3.4 2D array

By assuming a relatively constant material and plate thickness within a limited surface region, a 2D array defined by a group of sensors can be evaluated as a line array in the radial offset domain using a similar approach to that described in Section 3.2. This is done by adopting the transformation technique described in Section 3.3. One example of this evaluation is illustrated with the 2D array shown as blue markers in Fig. *5*(a). This 2D array is defined by the surface of a rectangle with a width

of 0.3 m and a slope of 25° (Fig. *5*(a)). The 2D array contains 85 sensors, and the data collected by these sensors are further studied in the radial offset domain. The surface in-plane acceleration response (r-direction) as function of time and space is shown in Fig. *5*(b). For improved readability, the presented time-domain data are low-pass filtered to reduce the frequency content above 30 kHz. In Fig. *5*(b), the longitudinal wave and the S1-ZGV Lamb mode can be observed; the data show major similarities with Fig. *3*(b).

The data are transformed to the frequency-phase velocity domain, and the results from this transformation are displayed in Fig. *5*(c). The processing technique required to create this correlation image is principally the same as that described in Section 3.2. However, since the data are analyzed in the radial offset domain, the coordinate variable x_m is replaced with the radial coordinate variable r_m. As a result, the test function for the discrete Fourier transform in the space domain takes a slightly different form, according to

$$\theta_{f-V}[r_m] = e^{2\pi i\, f_{test}/V_{test}\, r_m} \qquad \text{Eq. 12}$$

The corresponding test vector is created by

$$\boldsymbol{\theta}_{f-V} = \begin{bmatrix} \theta_{f-V}[r_1] \\ \theta_{f-V}[r_2] \\ \vdots \\ \theta_{f-V}[r_M] \end{bmatrix} \qquad \text{Eq. 13}$$

where r_m are the radial coordinates for the sensors. This means that the test vector $\boldsymbol{\theta}_{f-V}$ now represents a complex harmonic vector that is periodic along the radial axis r. Both the surface in-plane response (r-direction) and the surface normal response (z-direction) are calculated and used to create the correlation image in Fig. *5*(c) according to $(|s_{f-V,\mathrm{in-plane}}|+|s_{f-V,\mathrm{normal}}|)^2$. Major similarity between the correlation image for this 2D array (Fig. *5*(c)) and the correlation image for the line array (Fig. *3*(c)) is observed. This similarity ensures validity and strengthens the feasibility of using 2D arrays in evaluations performed in the radial offset domain. The similarity also verifies, to some extent, that the plate is homogenous within the measurement domain. This result is expected since a newly cast plate is studied; the test location is intentionally selected to ensure an environment with few uncertainties.

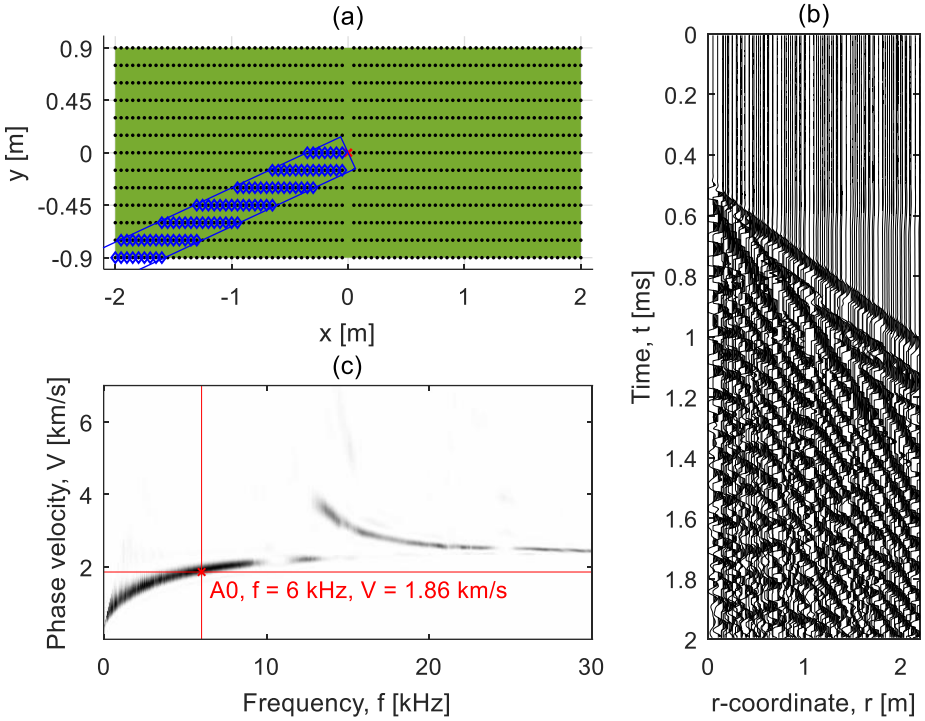

Fig. 5 (a) Measurement domain and rectangular 2D array shown with blue diamond markers, (b) time-domain low-pass filtered surface in-plane acceleration response, (c) frequency-phase velocity correlation image and estimated velocity for A0 Lamb mode at 6 kHz

3.5 Variation of phase velocity: polar angle and 2D imaging

The dispersive properties of Lamb modes in a plate are defined by the material properties and thickness. If a variation in the material or thickness is present in the lateral plane of the plate, then a variation in the dispersion is also present. The homogeneity of a plate can be assessed by measuring the phase velocity of Lamb modes at different locations on the plate. For a complete assessment, the analysis may be focused on the full frequency range of the dispersive wave field. However, this may be an elaborate task, at least for an initial assessment of a measurement object. It is therefore reasonable to select one or a few modes at a narrow range of frequencies for the initial analysis of homogeneity. As such example, in the following part of this study, we select the A0 Lamb mode at the frequency 6 kHz; see the marking with a red cross in Fig. *5*(c). This Lamb mode is selected since its mode shape is present through the entire thickness of the plate. The phase velocity of the mode is therefore dependent on both the material properties along the complete cross-sectional thickness as well as on the dimension of the thickness itself; i.e., the mode is not sensitive to potential local surface material inhomogeneities.

Using the test phase velocity that maximizes the correlation image amplitude at 6 kHz in Fig. *5*(c), the phase velocity for the A0 Lamb mode is estimated to be 1.86 km/s; see the marking with a red cross in Fig. *5*(c). The corresponding wavelength is therefore $\lambda = V/f \approx 0.3$ m. Thus, considering the nominal plate thickness of 0.12 m, this mode can be considered as a robust selection suitable for an initial assessment of the general homogeneity of the plate. The estimated phase velocity is representative of the surface region covered by the 2D array displayed with blue diamond markers in Fig. *5*(a). That is, the estimate represents a type of spatial average of the phase velocity for the mode within the surface region given by the 2D array; the 2D array can be interpreted as a spatial averaging operator dependent on the surface size and shape in relation to the wavelength of the mode.

Fig. 6(a) shows the estimated phase velocity for the A0 Lamb mode at 6 kHz as a function of the polar angle of the 2D array in steps of 5°. This result is obtained by a stepwise rotation of the 2D array in Fig. *5*(a) around the measurement and a corresponding estimation of the phase velocity at each step. Results show little variation in the estimated phase velocity; the minimum, mean, and maximum phase velocities are 1793 m/s, 1849 m/s, and 1911 m/s, respectively. That is, the variation is typically within $\pm 3\%$ of the mean phase velocity, and an almost consistent phase velocity for the A0 Lamb mode is observed. Thus, results from this initial assessment show that the plate is essentially homogenous within the measurement domain. This is expected since a newly cast plate is studied.

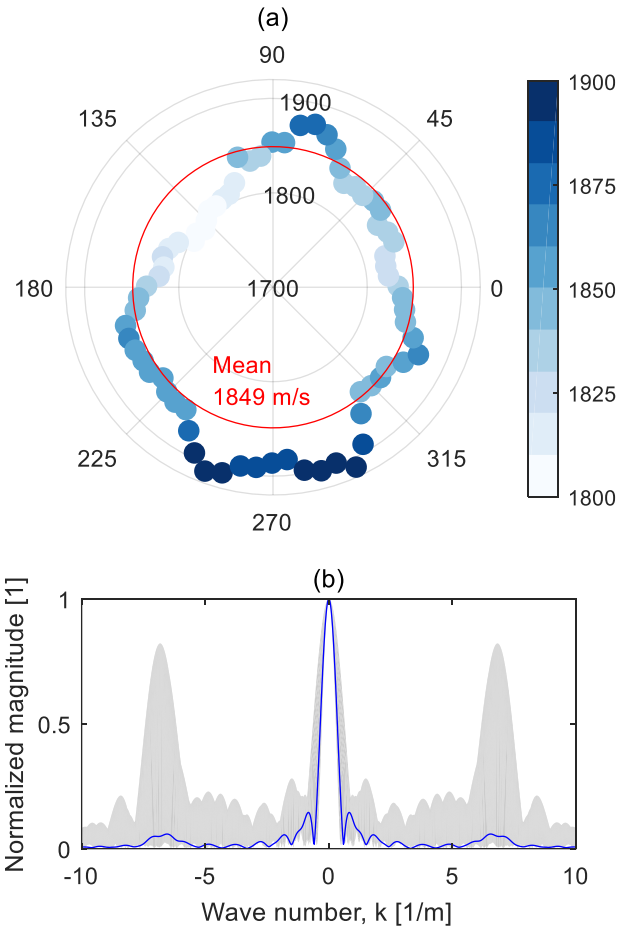

Fig. 6 (a) Estimated phase velocity for the A0 Lamb mode at 6 kHz as a function of polar angle for the rectangular 2D array; (b) envelope for normalized absolute values of the array window functions in frequency (wave number) domain shown as gray shading; blue line corresponds to rectangular 2D array in Fig. 5(a)

When performing a frequency analysis with discrete Fourier transforms, the topic of sampling is an important matter. In this example, where the phase velocity is estimated as a function of the angle of the 2D array, constant and uniform sampling is used in the time domain. However, this is not the case for sampling in the space domain, since each angle (step of 5°) is associated with one particular 2D array and set of sensors. This means that the number of sensors, as well as their interrelating locations in the radial offset (space) domain, will vary among the different 2D arrays (angles). For this reason, it is of interest to evaluate the influence from the characteristics of each 2D array (angle).

From a signal-processing point of view, a general array corresponds to a spatial window function that is used to sample the wave field [30]. The sampling in the radial offset (space) domain represents a

multiplication of the spatial array window function and the physical wave field. According to the convolution theorem, multiplication in the space domain corresponds to convolution in the frequency (wave number) domain. Thus, the measurement (sampling) corresponds to a convolution between the discrete Fourier transform of the array window function and the true wave field in the frequency domain. Owing to this, the resolution of the estimated phase velocity (wave number) is dependent on the discrete Fourier transform of the array window function. In this example, the array window is defined by a discrete rectangular function with unit value at the locations of the sensor positions and zero value elsewhere. This means that the spatial discrete Fourier transform of the array window function, at a test wave number $k_{test} = f_{test}/V_{test}$, is obtained by a summation of the complex components in the test vector $\boldsymbol{\theta}_{f-V}$ [26]. By repeating this calculation for a range of test wave numbers k_{test}, the spatial Fourier transform of the array window function is obtained.

For the 2D array shown with blue diamond markers in Fig. *5*(a), the absolute value of the spatial Fourier transform for the array window function is shown in Fig. *6*(b) with a blue solid line. The gray shading in Fig. *6*(b) represents the envelope corresponding to all 2D arrays that are used to create Fig. *6*(a). Note that the magnitude of the window functions are normalized in Fig. *6*(b). In the evaluation of the spatial Fourier transforms of window functions, two aspects are considered. The first aspect concerns the width of the main lobe at the wave number $k = 0$, which determines the resolution of the estimated frequency (wave number). A narrowing of this width increases the resolution and a broadening reduces the resolution. In Fig. *6*(b), the envelope exhibits some spread. From a manual inspection (not shown here) of the data analysis of the 2D arrays with the greatest main lobe width, we can see that reliable estimations of the phase velocity are obtained even for these 2D arrays. In particular, we verify that we can obtain correlation images (as in Fig. *5*(c)) with sufficient resolution and similarity compared with those created from the other 2D arrays with a narrower main lobe width. The second aspect concerns the locations of the highest side lobes, at $k = \pm 7$ in Fig. *6*(b), which provide information about potential aliasing. For the mean phase velocity of $V = 1849\ m/s$ at the frequency $f = 6\ kHz$, the corresponding wave number is $k = f/V = 3.2\ m^{-1}$. This means that the side lobes appear at $k = 3.2 \pm 7\ m^{-1}$. For the phase velocity, this corresponds to approximately $V = -1600\ m/s$ and $V = 600\ m/s$. Consequently, since the A0 Lamb mode is a single dominating mode at the investigation frequency (6 kHz), the effect from aliasing from these side lobes does not represent an issue in this example. To summarize, by considering these two aspects, we verify that the result presented in Fig. *6*(a) is based on a reliable sampling in space. This type of verification is central in all types of frequency analyses, but is especially important for the cases, as here, where nonuniform sampling is used.

The study of the variation in phase velocity in Fig. *6*(a) is made by rotating a 2D array with a rectangular shape. However, the rectangular shape represents only one among many possible shapes. For instance, a possible alternative is a 2D array defined by a circular surface. Fig. *7*(a) shows an example of a 2D array defined by a circle with radius 0.45 m, and this type of 2D array is further explored in the following. Compared with the rectangular 2D array in Fig. *5*(a), with one end fixed at the source location, Fig. *7*(a) shows that the position of a 2D array with a circular shape can be changed more freely within the measurement domain given by the green rectangle. Here, we sweep the circular 2D array within a rectangular grid space defined by 40 points along the x-axis and 20 points along the y-axis. Following the same principle as previously described, an estimation of the phase velocity for the A0 Lamb mode at 6 kHz is made at each grid point. Accordingly, this provides an estimate of the phase velocity over a 2D grid surface. The result from this evaluation is shown in Fig. *7*(c) as a phase velocity image with color corresponding to the estimated phase velocity. Note that the color of each pixel is representative of the estimated phase velocity within the complete surface covered by the corresponding 2D array. In other words, the pixel color does not represent a

pointwise phase velocity estimation, since the 2D array has an averaging (smoothing) influence. The minimum, mean, and maximum phase velocities are 1771 m/s, 1840 m/s, and 1910 m/s, respectively. Thus, also for this evaluation, an almost consistent phase velocity for the A0 Lamb mode is observed in the phase velocity image. Similar to the result in Fig. *6*(a), the phase velocity image in Fig. *7*(c) further confirms that a condition of material homogeneity and plate thickness is present in the measurement domain. Again, this result is expected since a newly cast and ideally homogenous plate is studied.

Similar to the evaluation based on a rotating 2D array, this evaluation is also associated with nonuniform sampling in the space domain. For the circular 2D array shown in Fig. *7*(a), the spatial Fourier transform of the corresponding array window function is shown with a solid blue line in Fig. *7*(b). The gray shading corresponds to the envelope of the spatial Fourier transforms of all array window functions. As previously, we verify the robustness of the estimation by monitoring the correlation image quality for the 2D arrays with the greatest main lobe. Again, since the A0 Lamb mode is a single dominating mode, the effect from aliasing due to side lobes does not present an issue in this case. Yet, for detailed and further investigations of an object, the implementation of a sampling criterion that discards estimates obtained from arrays with insufficient spectral resolution and performance may provide an approach for handling the sampling and ensuring consistent reliability of the results.

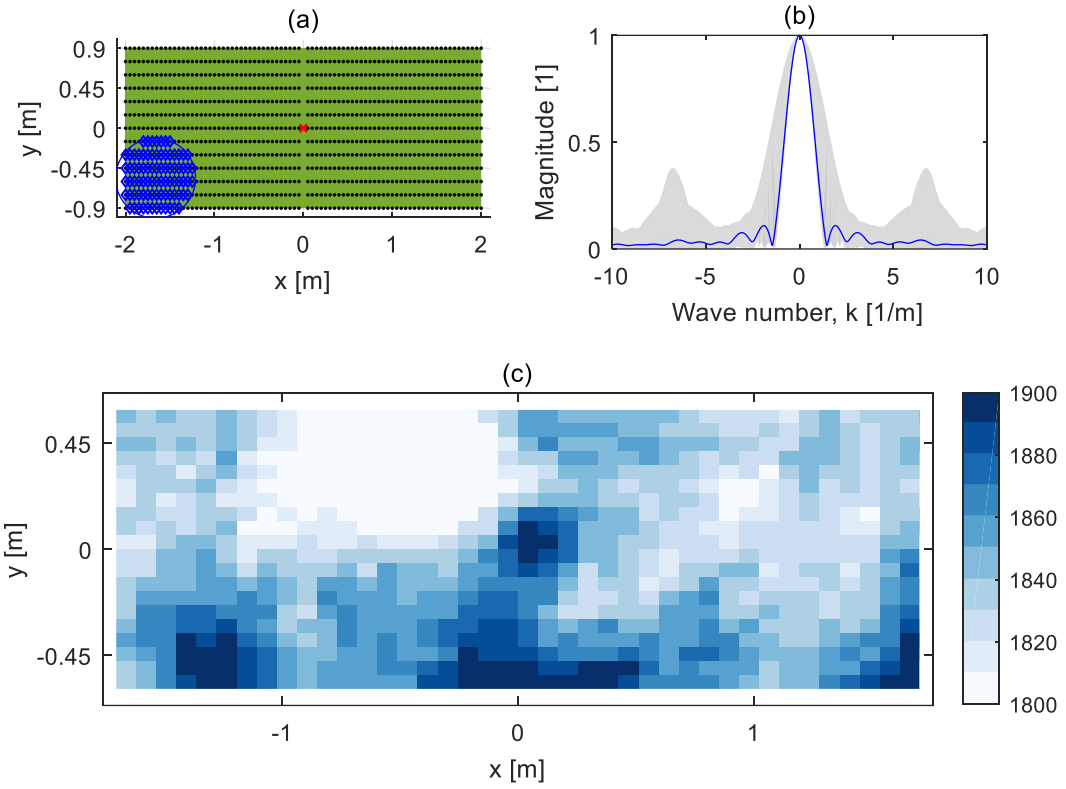

Fig. 7 (a) Measurement domain and circular 2D array shown with blue diamond markers; (b) envelope for normalized absolute values of the array window functions in frequency (wave number) domain shown as gray shading; blue line corresponds to circular 2D array in the top-left subfigure; (c) estimated phase velocity for the A0 Lamb mode at 6 kHz as function of 2D array center coordinate

4. Concluding remarks

With a full wave field dataset as the basis, we demonstrate and describe the implementation of a processing technique that enables a Lamb wave analysis in the frequency-phase velocity domain. Through the transformation of data into the radial offset domain, the initial technique is extended to include 2D arrays defined by 2D surfaces such as rectangles or circles. An analysis of the phase velocity as a function of polar angle is performed for 2D arrays with a rectangular shape, and a 2D phase velocity imaging analysis is performed for the 2D array with a circular shape. Naturally, other 2D array layouts are possible although they are not discussed here.

Results from the analysis of the phase velocity variation for the A0 Lamb mode at 6 kHz show a consistent phase velocity with little variation and a mean value around 1850 m/s. This means that the investigated plate is, as expected, essentially homogenous with little variation in the material properties and thickness within the measurement domain. Thus, this type of analysis is an example of an initial assessment of material condition and plate thickness for an unknown testing object. For most 2D arrays in this study, we used nonuniform sampling in the space domain. It is shown that a spectral estimation can also be performed under this sampling condition. Nevertheless, to ensure reliable results, the effect from the sampling condition should be evaluated.

The presented technique is demonstrated on one specific plate. Naturally, for further developments, it is important to investigate the application on other test objects as well as to understand its sensitivity to defects and anomalies. It is reasonable that the literature on guided wave applications in other fields may be useful for this task. Concerning the practicality of the measurements, it is expected that, with modern developments in fields such as wireless protocols, positioning systems, digital image processing, and augmented reality, the effort of collecting a full wave field dataset over a measurement domain, as in this study, can be minimized.

To summarize, from a general viewpoint we are able to show that a Lamb wave phase velocity imaging analysis of concrete plates can be performed with essentially the same simple equipment as that used for the IE method [7]. This highlights the very general characteristic of the utilized full wave field response, that a substantial number of evaluation methodologies are likely possible. Compared to ultrasonic transducers, transient impact sources are not limited to a narrow band of operating frequency; on the contrary, energy over a wide range of frequencies is generated and fed into a full wave field response. For this reason, techniques based on transient impact sources (full wave field) are important in cases where scattering and attenuation issues limit the use of ultrasonic techniques. In view of the need to inspect infrastructure constructions of large dimensions with potentially heavily reinforcement and coarse aggregates, we believe full wave field approaches, such as the one presented, represent a valuable and qualified complement to ultrasonic techniques. Here, it is emphasized that full wave field approaches operating in the frequency range below ultrasonic techniques, say 10–20 kHz, do not provide a substitute for ultrasonic techniques; our opinion is that optimal nondestructive evaluation is obtained by combining information from several techniques. That said, we hope that future full wave field approaches are considered equally qualified as ultrasonic techniques, and that this study provides a step toward a more developed and unified evaluation approach for concrete structures that utilize as many techniques (carriers of information) as reasonably possible.

Acknowledgements

The Development Fund of the Swedish Construction Industry (SBUF, No. 13104) and The Swedish Radiation Safety Authority (SSM, No. SSM2017-956) are acknowledged for financial support of the

study. The staff at PEAB in Trollhättan are acknowledged for generously providing access to the construction (test) site.

References

1. Bungey JH, Millard SG, Grantham MG (2006) Testing of Concrete in Structures, 4th ed. Taylor & Francis, Abingdon

2. Pla-Rucki GF, Eberhard MO (1995) Imaging of Reinforced Concrete: State-of-the-Art Review. J Infrastruct Syst 1:134–141. doi: 10.1061/(ASCE)1076-0342(1995)1:2(134)

3. Schickert M, Krause M, Müller W (2003) Ultrasonic Imaging of Concrete Elements Using Reconstruction by Synthetic Aperture Focusing Technique. J Mater Civ Eng 15:235–246. doi: 10.1061/(ASCE)0899-1561(2003)15:3(235)

4. Wiggenhauser H, Samokrutov A, Mayer K, et al (2016) Large Aperture Ultrasonic System for Testing Thick Concrete Structures. J Infrastruct Syst 23:B4016004. doi: 10.1061/(ASCE)IS.1943-555X.0000314

5. Almansouri H, Johnson C, Clayton D, et al (2017) Progress implementing a model-based iterative reconstruction algorithm for ultrasound imaging of thick concrete. AIP Conf Proc. doi: 10.1063/1.4974557

6. Schickert M, Krause M (2010) Ultrasonic techniques for evaluation of reinforced concrete structures. In: Non-Destructive Eval. Reinf. Concr. Struct. Elsevier, pp 490–530

7. Sansalone MJ, Streett WB (1997) Impact-echo: Non-destructive Evaluation of Concrete and Masonry. Bullbrier Press

8. Schubert F, Köhler B (2008) Ten Lectures on Impact-Echo. J Nondestruct Eval 27:5–21. doi: 10.1007/s10921-008-0036-2

9. Zhu J, Popovics JS (2007) Imaging Concrete Structures Using Air-Coupled Impact-Echo. J Eng Mech 133:628–640. doi: 10.1061/(ASCE)0733-9399(2007)133:6(628)

10. Dai X, Zhu J, Haberman MR (2013) A focused electric spark source for non-contact stress wave excitation in solids. J Acoust Soc Am 134:EL513-EL519. doi: 10.1121/1.4826913

11. Gibson A, Popovics JS (2005) Lamb Wave Basis for Impact-Echo Method Analysis. J Eng Mech 131:438–443. doi: 10.1061/(ASCE)0733-9399(2005)131:4(438)

12. Prada C, Clorennec D, Royer D (2008) Local vibration of an elastic plate and zero-group velocity Lamb modes. J Acoust Soc Am 124:203–212. doi: 10.1121/1.2918543

13. Kim DS, Seo WS, Lee KM (2006) IE-SASW method for nondestructive evaluation of concrete structure. NDT E Int 39:143–154. doi: 10.1016/j.ndteint.2005.06.009

14. Medina R, Bayón A (2010) Elastic constants of a plate from impact-echo resonance and Rayleigh wave velocity. J Sound Vib 329:2114–2126. doi: 10.1016/j.jsv.2009.12.026

15. Ryden N, Park CB (2006) A combined multichannel impact echo and surface wave analysis scheme for non-destructive thickness and stiffness evaluation of concrete slabs. AS NT, 2006 NDE Conf Civ Eng 247–253.

16. Barnes CL, Trottier J-F (2009) Hybrid analysis of surface wavefield data from Portland cement and asphalt concrete plates. NDT E Int 42:106–112. doi: 10.1016/j.ndteint.2008.10.003

17. Baggens O, Ryden N (2015) Systematic errors in Impact-Echo thickness estimation due to near

field effects. NDT E Int 69:16–27. doi: 10.1016/j.ndteint.2014.09.003

18. Medina R, Garrido M (2007) Improving impact-echo method by using cross-spectral density. J Sound Vib 304:769–778. doi: 10.1016/j.jsv.2007.03.019

19. Ryden N (2016) Enhanced impact echo frequency peak by time domain summation of signals with different source receiver spacing. Smart Struct Syst 17:59–72. doi: 10.12989/sss.2016.17.1.059

20. Baggens O, Ryden N (2015) Poisson's ratio from polarization of acoustic zero-group velocity Lamb mode. J Acoust Soc Am 138:EL88-EL92. doi: 10.1121/1.4923015

21. Boiero D, Bergamo P, Rege RB, Socco LV (2012) Estimating surface-wave dispersion curves from 3D seismic acquisition schemes : Part 1 — 1D models. Geophysics 76:G85–G93. doi: 10.1190/geo2011-0124.1

22. Harley JB, Moura JMF (2013) Sparse recovery of the multimodal and dispersive characteristics of Lamb waves. J Acoust Soc Am 133:2732–2745. doi: 10.1121/1.4799805

23. Park CB, Miller RD, Xia J (1999) Multichannel analysis of surface waves. Geophysics 64:800–808. doi: 10.1190/1.1444590

24. Gao W, Glorieux C, Thoen J (2003) Laser ultrasonic study of Lamb waves: Determination of the thickness and velocities of a thin plate. Int J Eng Sci 41:219–228. doi: 10.1016/S0020-7225(02)00150-7

25. Alleyne D, Cawley P (1991) A two-dimensional Fourier transform method for the measurement of propagating multimode signals. J Acoust Soc Am 89:1159–1168. doi: 10.1121/1.400530

26. Zywicki D, Rix G (2005) Mitigation of near-field effects for seismic surface wave velocity estimation with cylindrical beamformers. J Geotech Geoenvironmental … 970–977. doi: 10.1061/(ASCE)1090-0241(2005)131:8(970)

27. McMechan GA, Yedlin MJ (1981) Analysis of dispersive waves by wave field transformation. Geophysics 46:869–874. doi: 10.1190/1.1441225

28. Park CB, Miller RD, Xia J, Survey KG (1998) Imaging dispersion curves of surface waves on multichannel record. In: 68th Ann. Internat. Mtg., Soc. Expl. Geophys. Expand. Abstr. pp 1377–1380

29. Ambrozinski L, Piwakowski B, Stepinski T, Uhl T (2014) Evaluation of dispersion characteristics of multimodal guided waves using slant stack transform. NDT E Int 68:88–97. doi: 10.1016/j.ndteint.2014.08.006

30. Brandt A (2011) Noise and Vibration Analysis. doi: 10.1002/9780470978160

Appendix D

Paper IV

O. Tofeldt and N. Ryden. 2017.
Zero-group velocity modes in plates with continuous material variation through the thickness. The Journal of the Acoustical Society of America, 141(5):3302-3311.
DOI: 10.1121/1.4983296

Zero-group velocity modes in plates with continuous material variation through the thickness

Oskar Tofeldt[a] and Nils Ryden
Division of Engineering Geology, Lund University, P.O. Box 118, SE-22100, Lund, Sweden

(Received 29 December 2016; revised 27 April 2017; accepted 28 April 2017; published online 17 May 2017)

Lamb modes with zero group velocity at nonzero wave numbers correspond to local and stationary resonances in isotropic plates. Lamb modes can be utilized for nondestructive evaluation of the elastic properties and thickness. One example of an application is the testing of plate-like concrete structures. In this example, continuous variation in the material velocity through the thickness may occur. This is usually not accounted for in analyses, and with this as starting point, two inhomogeneous and nonsymmetric cases with continuous material variations are investigated using a semi-analytical finite element technique and a simulated measurement application. In a numerical study limited to the lowest zero-group velocity mode, results show that these modes for the inhomogeneous cases are generated with similar behavior and the same detectability as in the case of an isotropic plate. However, a complex relationship between mode frequency and material velocity exists for the inhomogeneous cases. This hinders the evaluation and interpretation of representative estimations such as those for a cross-sectional mean value of the plate properties. This may lead to errors or uncertainties in practical applications. © *2017 Acoustical Society of America*.
[http://dx.doi.org/10.1121/1.4983296]

[JFL] Pages: 3302–3311

I. INTRODUCTION

An interesting and fascinating type of Lamb mode is the so-called zero-group velocity (ZGV) mode.[1,2] These Lamb modes possess the extraordinary property of a vanishing group velocity combined with a nonzero wave number. More specifically, the vanishing group velocity is due to the interference of two modes, defined at the same frequency, that have the same mode shape propagating with equal absolute phase velocities (wave numbers) but with opposite signs (directions). In this case, a stationary mode is obtained that materializes as a local ringing resonance of the plate structure with a sharp and distinct frequency peak in the response spectrum. Since the characteristics of ZGV Lamb modes are defined by the elastic properties and thickness of the plate,[3] this type of resonance may be utilized for nondestructive evaluation. Because of its stationary and nonpropagating nature, a local estimation of the elastic properties and thickness is obtained.[1,4] This feature is particularly useful in situations where constant material or thickness is not ensured in the lateral plane of the plate and in cases where a free and accessible surface for analyzing propagating waves is limited.

In the literature, Tolstoy and Usdin[5] predicted in 1957 the existence of a sharp ringing resonance related to a vanishing group velocity in an elastic plate. More recently, the topic has received new attention in studies that demonstrate both generation and detection of such sharp ringing resonances[4,6] and explicitly link this phenomena to ZGV Lamb modes. The topic of ZGV Lamb modes is currently active within ongoing nondestructive evaluation studies. Topics include isotropic plates,[1,7,8] anisotropic plates,[9] hollow cylinders,[10,11] the interfacial stiffness of layered media,[12,13] thin-layer measurements,[14] and glass materials.[15] Studies also examine air-coupled measurements,[4,16–18] wave focusing,[19,20] and enhanced ZGV Lamb mode generation in laser ultrasonic applications.[21–23]

Clearly, the results presented in the literature demonstrate the potential of using ZGV Lamb modes, and several evaluation techniques and applications have evolved. One example, which is the focus of the present work, is the testing of plate-like concrete structures. Early studies reported on the usage of a longitudinal thickness resonance,[24] which is linked to the first symmetric ZGV Lamb mode[25] and subsequently combined with surface wave measurements.[26] More recently, this work has been extended with techniques that use the ZGV Lamb mode shape to estimate the temporal frequency[27–29] and Poisson's ratio.[7] Indeed, this example of progression confirms and strengthens the importance of a thorough understanding of the behavior of ZGV Lamb modes for improved further development.

Although the literature concerning ZGV Lamb modes is rather extensive, to the authors' best knowledge, only a few studies consider the topic of continuously varying material through the plate thickness.[30] In contrast to structures formed by discrete layers and well-defined interfaces such as laminates, some plate-like concrete structures may have continuously varying material properties through the plate thickness.[31–37] Such continuous material variations, resulting in varying acoustic bulk wave velocities, may originate from the uneven settlement of aggregates during casting, uneven moisture distribution, material degradation or corrosion of internal steel reinforcement, or other mechanisms.[38] Even so, potential variations in the material properties are

[a]Electronic mail: oskar.tofeldt@tg.lth.se

 0001-4966/2017/141(5)/3302/10/$30.00

generally not considered in measurements of plate-like concrete structures with ZGV Lamb modes;[25,39] on the contrary, isotropy based on constant material properties through the plate thickness is usually implicitly assumed. To better understand the limitations and robustness of this type of application and to support further development, there is a need for improved knowledge of ZGV Lamb modes in plates with continuous material variations through the thickness. Improved understanding also contributes to the overall aim of increased knowledge within the general field of ZGV Lamb modes.

This study investigates the behavior of ZGV modes in two synthetic cases defined by two plates with inhomogeneous and nonsymmetric continuous variation of the acoustic bulk wave velocities. Results are also compared with a corresponding isotropic case. Since only a few prior studies used higher ZGV modes in the testing of plate-like concrete structures,[40,41] the present work is limited to a study of the lowest ZGV mode. For isotropic plates with Poisson's ratio $\nu < 0.45$, the lowest ZGV mode is linked to the first symmetric (S1) Lamb mode,[1] typically referred to as the S1-ZGV Lamb mode. The study is organized in sections as follows: Sec. II defines the material variation cases, Sec. III describes the investigation into the cases using a semi-analytical finite element (SAFE) technique, and Sec. IV further explores the cases in a simulated nondestructive testing application. Although the study originates from a perspective of thick concrete structures, the results hold for other inhomogeneous cases as well under the condition of guided wave propagation in plate-like structures through the general assumption of linear elastic wave propagation.

II. MATERIAL VARIATION CASES

This study investigates two inhomogeneous cases, referred to as case 1 and case 2, defined by two infinite plates with continuous material variation throughout the thickness. These two cases (plates) are also compared with a homogeneous, isotropic reference case defined by an isotropic and infinite plate with constant material properties throughout its thickness. Although the unbounded (infinite) domain of the cases represent a theoretical and idealized condition, results for the lowest ZGV Lamb mode derived under this assumption can be generalized and extended to real plates of finite dimensions at distances greater than one thickness from the plate-edge.[42] From the perspective of thick plate-like concrete structures that may have continuous material variations, cases 1 and 2 are characterized by a continuous inclusion of material with a high and low acoustic wave velocity, respectively. A more detailed description of both cases and their relation to the isotropic reference case is provided below.

Both cases are modifications of the isotropic reference case, which is represented by a linear elastic isotropic plate with thickness axis parallel to the vertical z axis, infinite lateral dimensions in the horizontal xy plane, a midplane coincident with the horizontal xy plane ($z = 0$), and a thickness $t = 1$ m. The homogeneous material in the isotropic reference case is defined by a longitudinal wave velocity $V_L = 4303$ m/s, a transversal wave velocity $V_T = 2635$ m/s (Poisson's ratio $\nu = 0.2$), and density $\rho = 2400\,\mathrm{kg/m^3}$. Starting from this isotropic reference case as a common basis, case 1 and case 2 are generated by adjusting the values of the acoustic bulk wave velocities ($V_L = 4303$ m/s and $V_T = 2635$ m/s) according to a scaling function with spatially varying amplitude along the plate thickness coordinate z.

In total, two scaling functions are used in the study with one function assigned to each case. The scaling functions for case 1 and case 2 are shown in Figs. 1(a) and 1(b), respectively. The two functions are defined similarly, with one term given by a single cycle of a sinusoidal function

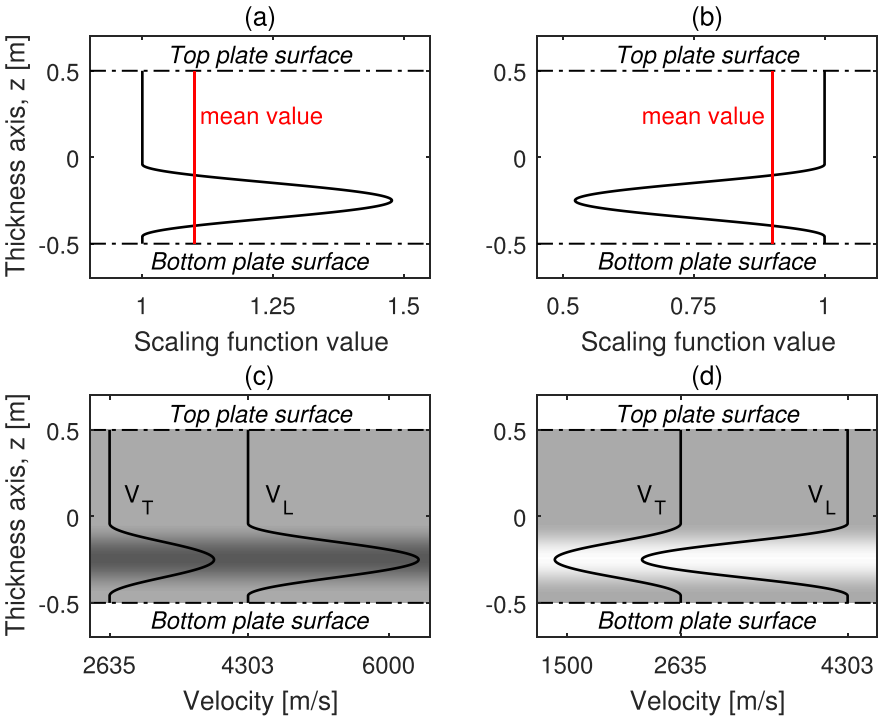

FIG. 1. (Color online) Scaling function for (a) case 1 and (b) case 2. Variation of acoustic bulk wave velocities for (c) case 1 and (d) case 2.

(crest to crest) as well as a second constant term of unity. For both cases, the wave cycle has the same frequency and spatial location but it differs in magnitude and sign. The corresponding variations in the longitudinal and transversal wave velocities as function of the thickness coordinate for cases 1 and 2 are shown in Figs. 1(c) and 1(d), respectively. To highlight the continuous variation of the material, the darkness of the background colors of Figs. 1(c) and 1(d) increase with increasing velocity. It is emphasized that, since the longitudinal and transversal wave velocities vary with the same shape and relative magnitude, a uniform value of the Poisson's ratio ($\nu = 0.2$) is maintained throughout the entire thickness of the plate in both cases. It can also be noted that, for both cases, the material at the top and bottom plate surfaces is unaffected by the scaling function and accordingly remains the same.

Figure 1 shows that cases 1 and 2 represent an increase and decrease in the magnitude of the acoustic bulk wave velocities, respectively. For both cases, this shift appears in a region below the midplane of the plate ($z < 0$) and is symmetric around a peak value located at $z = -0.25$. At this peak value, cases 1 and 2 exhibit an increase and decrease, respectively, of the acoustic bulk wave velocities with a maximum absolute relative change of approximately 50%. More precisely, the specific amplitudes of the sinusoidal wave cycles for both cases are adjusted to result in a relative shift of 10% of the spatial mean acoustic bulk wave velocities throughout the plate thickness, compared to the initial values defined by the isotropic reference case ($V_L = 4303$ m/s and $V_T = 2635$ m/s). This relative shift is highlighted in Figs. 1(a) and 1(b) by the cross-sectional mean value of the scaling functions (0.9 and 1.1) for case 1 and case 2, respectively.

Considering the above detailed descriptions of the two cases, it should be noted that these two cases represent just one selection from the countless candidate material variation cases. In fact, an infinite number of material variation cases exist. With the necessity to limit these cases, the present work focuses on two cases that enable a study of ZGV modes in plates with a continuous inclusion of material with either high or low acoustic bulk wave velocities. Moreover, the inclusion is located in a position that creates a nonsymmetric inhomogeneous material condition with respect to the midplane of the plate. Although the motive for this selection develops from the perspective of thick concrete structures, it should be noted that the cases are not representative of a particular concrete structure or of a universal material variation case. However, given the high magnitude of variation in the acoustic bulk wave velocities, it is anticipated that most concrete structures fall within the boundary limits formed by the case definitions. As a result, the observed qualitative and quantitative results can be considered valuable and relevant for plate-like concrete structures in general as well as for other ZGV Lamb mode applications in view of the general validity of linear elastic wave propagation.

III. SEMI-ANALYTICAL FINITE ELEMENT ANALYSIS

A. Method

Under the assumption of a linear elastic, isotropic, and infinite plate located in the horizontal xy plane, the vertically (z axis) polarized wave field is defined by the Rayleigh-Lamb equation;[3,43,44] the corresponding solutions in terms of wave modes are usually referred to as Lamb modes. Although the Rayleigh-Lamb equation appears in a deceivingly simple and compact form, the task of obtaining a full wave field solution usually requires extensive processing. As anticipated, the case of layered structures is more complex than the case of isotropic plates. For most layered structures, closed form equations like the Rayleigh-Lamb equation do not exist. Instead, global matrix formulations based on discrete isotropic layers joined by common interfaces may be adopted.[45] Typically, these approaches, often referred to as matrix methods, are used for systems described by a handful of layers.

In the study of mechanical waves in plates with continuous material variations, such as with cases 1 and 2, conventional finite element (FE) simulations can be used to predict the dynamic response behavior. However, data from such simulations simultaneously include all existing wave modes within the investigated frequency range; thus, extensive processing is usually required to resolve the dispersive relations within the wave field solution. An alternative approach is to adopt a SAFE technique,[46] which is a compromise between a fully numerical method and a strictly analytical method. Briefly, the SAFE technique assumes harmonic wave mode propagation along the path of a uniform waveguide defined by an arbitrary, but constant, cross section in the lateral direction. A reduced system is obtained in which only the waveguide cross section must be discretized by finite elements. The wave field solution of the system can then be determined by solving the associated eigenvalue problem of temporal and spatial frequency using standard numerical routines. On that account, the SAFE technique is one possible candidate approach for obtaining the wave field solution of cases 1 and 2; therefore, it is adopted in the present work.

From the implementation of a SAFE model in a commercial FE code,[47] as described by Predoi *et al.*,[48] the wave field solutions for cases 1 and 2 are determined and further analyzed. These wave field solutions, strictly speaking, are determined from a model composed of a finite number of discrete material layers (elements). However, by including a sufficient number of material layers (elements) and with a careful monitoring of the model solution convergence, the obtained wave field solutions approach the continuous nature of cases 1 and 2. The wave field solution for the isotropic reference case is also determined. For all three cases (1, 2, and the isotropic reference), no material damping is taken into account.

B. Results and analysis

The resulting wave number-frequency dispersion curves for cases 1 and 2 obtained from the SAFE model are shown in Figs. 2(a) and 2(b), respectively. The dispersion curves in Fig. 2 show the four lowest propagating modes (real wave number k) polarized in the plane defined by the thickness axis (z) and the lateral propagation axis; no shear horizontal modes are displayed. These four modes are denoted M1, M2, M3, and M4 for both cases (see Fig. 2). The dispersion

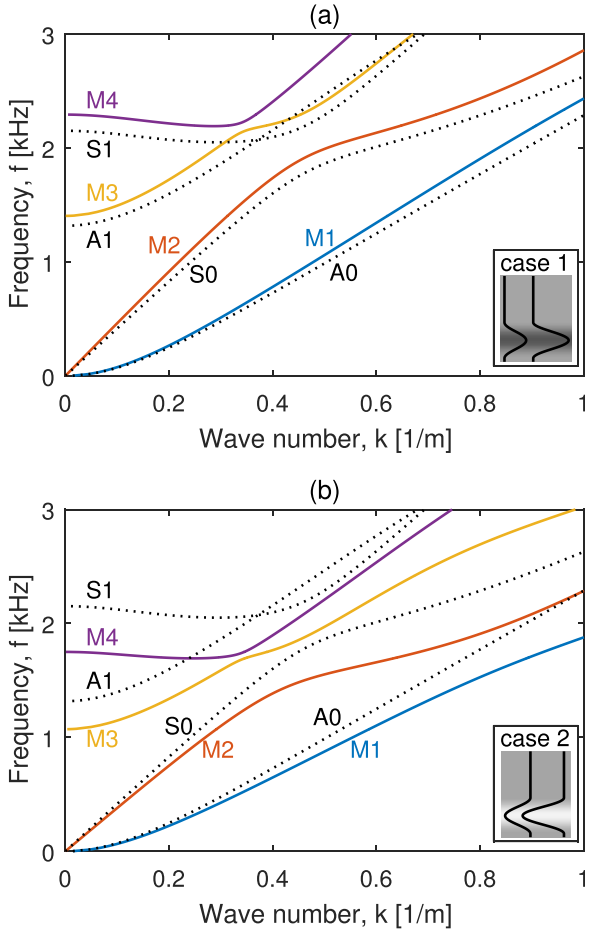

FIG. 2. (Color online) Wave number frequency solution for (a) case 1 and (b) case 2. Dotted lines show the isotropic reference case.

curves for the four lowest Lamb modes for the isotropic reference plate, A0, S0, A1, and S1, are displayed for comparison (dotted lines). For both cases, Fig. 2 shows that the overall pattern exhibited by the M1–M4 modes is similar to the pattern exhibited by the A0, S0, A1, and S1 Lamb modes for the isotropic reference plate. Moreover, it can be observed that, in general, the M1–M4 modes for case 1 [Fig. 2(a)] display a higher temporal frequency f at a given wave number k compared to the corresponding Lamb modes for the isotropic reference case at the same wave number k. This increase in frequency is equivalent to an increase in phase velocity $V_{\mathrm{ph}} = f/k$ and is due to the increase in the mean acoustic bulk wave velocities as defined by the scaling function associated with the case. As shown in Fig. 2(b), the opposite situation, with decreased frequency and phase velocity due to a decrease in the mean acoustic bulk wave velocities, holds for case 2.

Although both case 1 and case 2 exhibit similarities with the isotropic reference case, one difference between cases 1 and 2 and the isotropic reference case is that the M3 and M4 modes do not cross each other whereas the A1 and S1 Lamb modes do cross.[49,50] This important difference occurs because the wave field solution of an isotropic plate is divided into two families consisting of symmetric and antisymmetric modes with respect to the midplane of the plate. These two types of mode families are uncoupled through two separate governing equations.[3] However, for both case 1 and case 2, no such symmetry plane exists; i.e., no strict separation into symmetric or antisymmetric modes can be made and, therefore, crossings between the modes Mn within cases 1 and 2 are not allowed due to mode repulsion.[51] This lack of separation into symmetric or antisymmetric modes provides the motivation for the naming convention of the modes in cases 1 and 2 (M1, M2, …, Mn); i.e., no strict classification according to symmetry is made.

To facilitate the study of the first ZGV mode, an expanded view within a narrower range of wave numbers and frequencies is created (Fig. 3). Figure 3 shows the M4 mode wave number-frequency dispersion curves for cases 1 and 2 as well as the corresponding S1 Lamb mode curve for the isotropic reference plate. For both case 1 and case 2, it can be observed that the M4 dispersion curves, similar to the S1 dispersion curve, exhibit minimum points at a nonzero wave number. These minimum points, marked with asterisks in Fig. 3, represent modes at which the group velocity vanishes $V_g = df/dk = 0$; i.e., they are ZGV modes. For this reason, they are referred to as M4-ZGV and S1-ZGV (Fig. 3).

The frequencies f of the M4-ZGV mode for case 1 and case 2 are 2192 and 1694 Hz, respectively. Comparing with the frequency $f = 2051$ Hz for the S1-ZGV Lamb mode for the isotropic reference case, two observations are made. First, the shift in frequency is not linearly proportional to the change in the cross-sectional mean value of the acoustic bulk wave velocities ($+-10\%$). Second, the frequency f increases by 7% and decreases by 17% for case 1 and case 2, respectively, which indicates that the magnitude of the relative shift differs between the cases.

Regarding the first observation, this result is different for an isotropic plate where a relative shift in the acoustic bulk wave velocities is reflected as the same relative shift in frequency under the condition of a constant Poisson's ratio. Because of this, the explanation and description of the S1-ZGV Lamb mode frequency for isotropic plates is occasionally simplified to the empirical equation

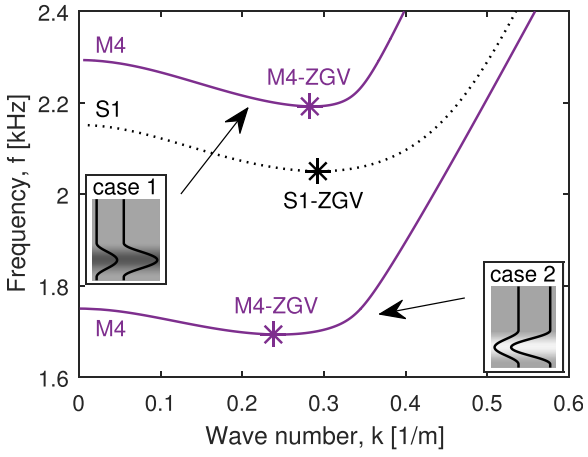

FIG. 3. (Color online) Expanded view of wave number frequency solution for the M4 mode (both case 1 and case 2) and S1 Lamb mode (isotropic reference case, dotted line). ZGV points marked with asterisks.

$$f = \frac{\beta V_L}{2h}, \tag{1}$$

where β is a correctional factor only dependent on the Poisson's ratio[25] and $V_L/(2h)$ represents the frequency of a cutoff mode created by a reverberating longitudinal wave. In more detail, Eq. (1) may be ascribed to the simplified and empirical interpretation[24] of the S1-ZGV Lamb mode as a reverberating longitudinal wave with a frequency shifted by the factor β. Although Eq. (1) produces the correct value of the S1-ZGV Lamb mode frequency, note that this interpretation is rather deceptive since Lamb waves, except at the mode cutoff, by definition are always created from the interference of both longitudinal and transversal waves. This explains the need for the correctional β factor, which in any event requires that the original Lamb wave problem is solved. Moreover, for plates with a Poisson's ratio $\nu > 1/3$, the cutoff S1 Lamb mode is created by a transversal wave as opposed to a longitudinal wave. In view of that, the meaning of Eq. (1) becomes somewhat ambiguous.

Regarding the second observation, a simplified and partial explanation for the difference in the relative shift of frequency (7% vs 17%) may be determined from the time of flight required for a high-frequency pulse with finite duration in time and space to travel between the top and bottom plate surface.[24] By comparing this time of flight for cases 1 and 2 with the corresponding value for the isotropic reference case, it can be shown that case 1 exhibits less relative change than case 2. Although this agrees with the result of the relative shift of the M4-ZGV frequency, note that this simplified analysis does not provide a consistent quantitative estimate of the frequency shift of the M4-ZGV mode compared with the S1-ZGV Lamb mode.

Certainly, due to the inhomogeneous variation of the acoustic bulk wave velocities in cases 1 and 2, no simple empirical expression like Eq. (1) exists; for both case 1 and case 2, there is a complex relation between mode frequency and acoustic material velocity. Indirect consequences of this additional complexity compared to the isotropic reference case may appear in nondestructive evaluations of the plate properties. For instance, if an isotropic Lamb wave model is assumed under the actual condition of case 1 or 2, then the estimated acoustic material velocity or plate thickness[39] from the M4-ZGV mode will be difficult to interpret since it cannot be directly translated to a representative mean value or other similar established quantitative measure. A similar argument holds for the shift in wave number or wavelength for the M4-ZGV mode.

Figure 4 shows the displacement mode shapes of the M4-ZGV mode (asterisks in Fig. 3) for case 1 and case 2 as a function of the plate thickness coordinate z. The profiles of the vertical and horizontal displacements are shown in Figs. 4(a) and 4(b), respectively. The corresponding displacement profiles of the S1-ZGV Lamb mode for the isotropic reference case are also shown for comparison (black dots). The amplitude of the profiles is normalized to produce the same maximum magnitude for all profiles. For both case 1 and case 2, Fig. 4 shows slightly distorted mode shapes—in contrast to the isotropic reference case—as there

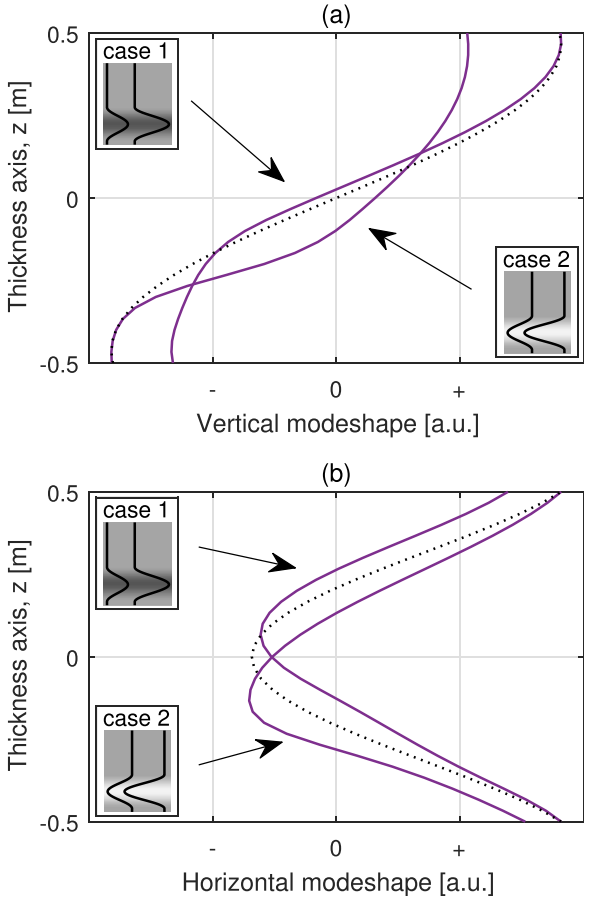

FIG. 4. (Color online) Displacement mode shape of the M4-ZGV mode for case 1 and case 2 (a) in the vertical direction and (b) in the horizontal direction. Dotted lines show S1-ZGV from the isotropic reference case.

is no strict symmetry around the midplane of the plate. The location of the neutral planes, in this case interpreted as the coordinate in the cross section with zero displacement magnitude, is also different for the two cases. For cases 1 and 2, the neutral planes are shifted toward the top surface ($z = h/2$) and bottom surface ($z = -h/2$) of the plate, respectively. Nonetheless, it can be concluded that the overall characteristic is roughly the same for the M4-ZGV mode as for the S1-ZGV Lamb mode, and loosely speaking, the M4-ZGV mode shape for both cases may be approximately symmetric. To summarize, for both cases, the M4-ZGV mode and the S1-ZGV Lamb mode both have a mode shape that persists throughout the entire plate thickness. This means that the mode may represent the entire thickness, in contrast to Rayleigh type of waves that only reflect the localized properties of the surface. In addition, the stationary nature of ZGV modes imply that estimations are locally representative in the lateral plane of the plate, since they are not influenced by any lateral propagation path.

Although the general pattern of the dispersion curves for case 1 and 2 and the isotropic reference case have apparent similarities, the behavior of an isotropic plate cannot always be extrapolated to cases such as case 1 and 2. For instance, by studying the M4 mode shape for increasing wave number k in a region close to the M4-ZGV point, it can be observed

that the M4 mode shape characteristic for both cases 1 and 2 changes from approximately symmetric to approximately antisymmetric close to the M4-ZGV mode frequency. The opposite holds for the M3 mode, which evolves from approximately antisymmetric to approximately symmetric for both cases 1 and 2. In other words, an interchange in characteristic mode shape between the M3 and M4 modes occurs in a region close to the M4-ZGV point. This type of interchange in mode behavior, sometimes referred to as mode kissing, is for both cases caused by the lack of symmetry around the midplane of the plate due to inhomogeneous material variation.

Traditionally, the group velocity of a wave mode is defined as the slope of the dispersion curve, i.e., $V_g = df/dk$. However, obtaining a stable continuous differentiation of the dispersion curves with respect to wave number may occasionally become difficult due to the discrete nature of the numerical solution. An alternative approach, adopted in this study, is to calculate the so-called energy velocity of the wave mode, since these two quantities are coincident for plates without material attenuation.[52] Using this approach, the group velocity (energy velocity) is determined from $V_e = P/E_{\text{tot}}$, where P is the one-period time and cross-section-averaged Poynting vector component in the propagation direction of the mode, and E_{tot} is the one-period time and cross-section-averaged total (kinetic and potential) energy of the wave mode.[46] Figures 5(a) and 5(b) show the group velocity (energy velocity) of the M1–M4 modes for case 1 and case 2, respectively. The group velocity (energy velocity) of the four lowest Lamb modes for the isotropic references case is also shown for comparison. For both case 1 and case 2, the M4-ZGV mode materializes in a similar manner as for the isotropic case. The shift in frequency for the M4-ZGV mode, in terms of a horizontal translation of the M4 curve compared to the isotropic reference case, is also clearly visible for both cases.

The excitability of the four lowest M1–M4 modes for case 1 and case 2 is displayed in Figs. 6(a) and 6(b), respectively. The excitability of the four lowest Lamb modes for the isotropic reference case is shown for reference. Similar to that in Fig. 5, a general shift in frequency, revealed as a horizontal translation of the M4 excitability curve, can be observed in Fig. 6 for both cases. Here, note that the excitability is interpreted as the displacement magnitude at the top surface of the plate in the surface normal direction, caused by a unit point load applied at the same point and direction. More specifically, excitability is calculated according to $E = i\omega|U|^2/(4P)$, where ω is the angular frequency, U is the surface normal displacement at the top surface of the plate, and P is the one-period time and cross-section-averaged Poynting vector component in the propagation direction of the mode.[53] Figure 6 shows that the M4 curves for both case 1 and case 2 exhibit high values of excitability around the M4-ZGV mode frequency. Accordingly, these results suggest that high displacement amplitudes, in the form of a local resonance of the plate, are to be expected at the top plate surface even in these two cases subjected to continuous inhomogeneous material variations. For this reason, the robustness and detectability

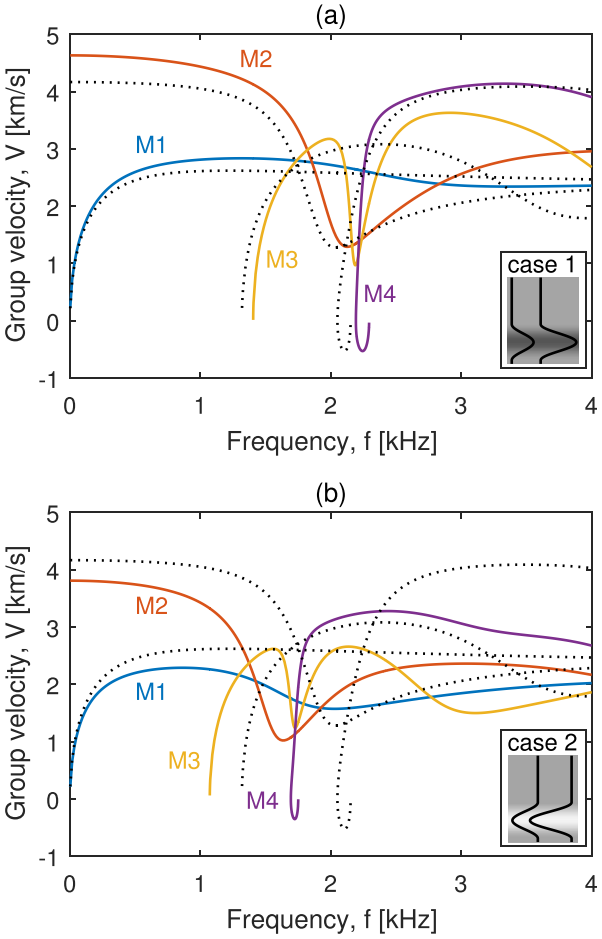

FIG. 5. (Color online) Group velocity for (a) case 1 and (b) case 2. Dotted lines show isotropic reference case.

of the M4-ZGV mode frequency in a nondestructive application is studied using a simulation, as discussed in Sec. IV.

IV. SIMULATION OF MEASUREMENT APPLICATION

A. Description of application

Similar to the S1-ZGV Lamb mode for the isotropic reference case, results from the SAFE analysis in Sec. III suggest that high displacement amplitudes at the top plate surface are expected at the M4-ZGV mode frequency for case 1 and case 2. This predicted behavior is simulated in an application corresponding to a nondestructive measurement and evaluation technique; furthermore, simulation results can be used to verify the results from the SAFE analysis. Considering the original motive for case 1 and case 2, the application is selected to represent a measurement of plate-like concrete structures.[26,39] In this type of measurement, an accelerometer is attached to the top plate surface. Then, the vibration response from hammer impacts, performed at an increasing offset distance from the accelerometer, is recorded. Since the hammer also works as a triggering device, reciprocity is used to create a multi-signal recording of a full wave field response from a single-point source excitation. In fact, such a multi-signal recording representing a

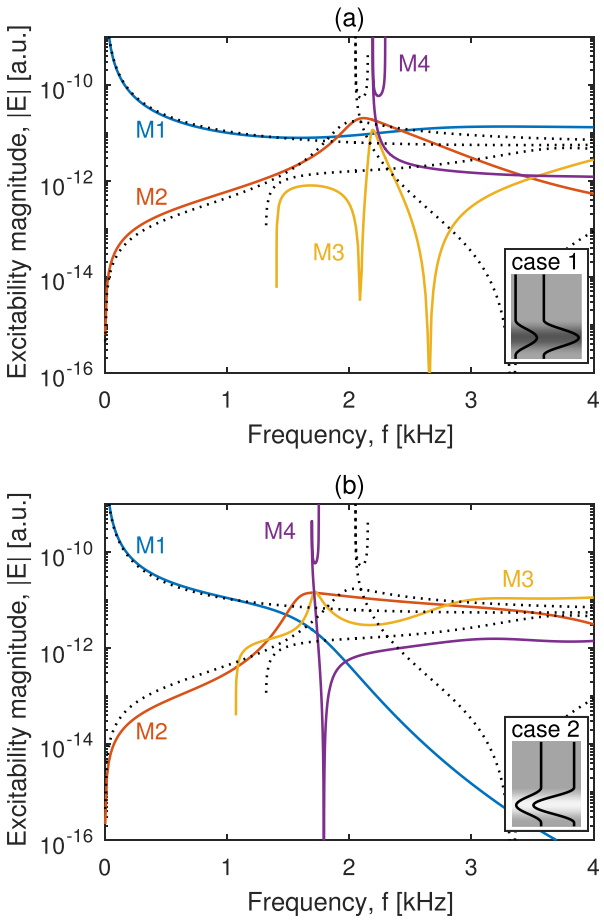

FIG. 6. (Color online) Excitability for (a) case 1 and (b) case 2. Dotted lines show isotropic reference case.

very general type of data set can be found in a number of applications.

B. Model and analysis

A two dimensional (2D) conventional FE model created in a commercial code[47] is used to study cases 1 and 2 and the isotropic reference case. The cases are modeled as a 10 m long plate with an axial symmetry condition that enables a point source excitation from a hammer impact. At the farther end of the plate, away from the axial symmetry axis and point source excitation, an absorbing region is added to reduce reflections from the plate end boundary.[54] This allows a finite approximation of the infinite lateral (radial) dimension according to the case definition to be obtained. In addition to the absorbing region and the geometrical damping caused by the axial symmetry condition, material damping is also introduced by a loss factor $\eta = 0.02$. The point source excitation is applied as a Gaussian mono-pulse with a center frequency corresponding to the S1-ZGV Lamb mode frequency; a broadband excitation, similar to that from a hammer impact, is obtained. Then, synthetic data sets represented by the time-domain acceleration response of the top plate surface are determined from the inverse Fourier transform of the model response in frequency domain.[55]

The acceleration response as function of time at different radial offset distances to the hammer impact for cases 1 and 2 are shown in Figs. 7(a) and 7(c), respectively. These figures show an expanded view of the data sets within a time range 0–5 ms and a radial offset distance range 0–2 m for cases 1 and 2, respectively. Here, the radial coordinate $r = 0$ m corresponds to the impact location. To estimate the wave number-

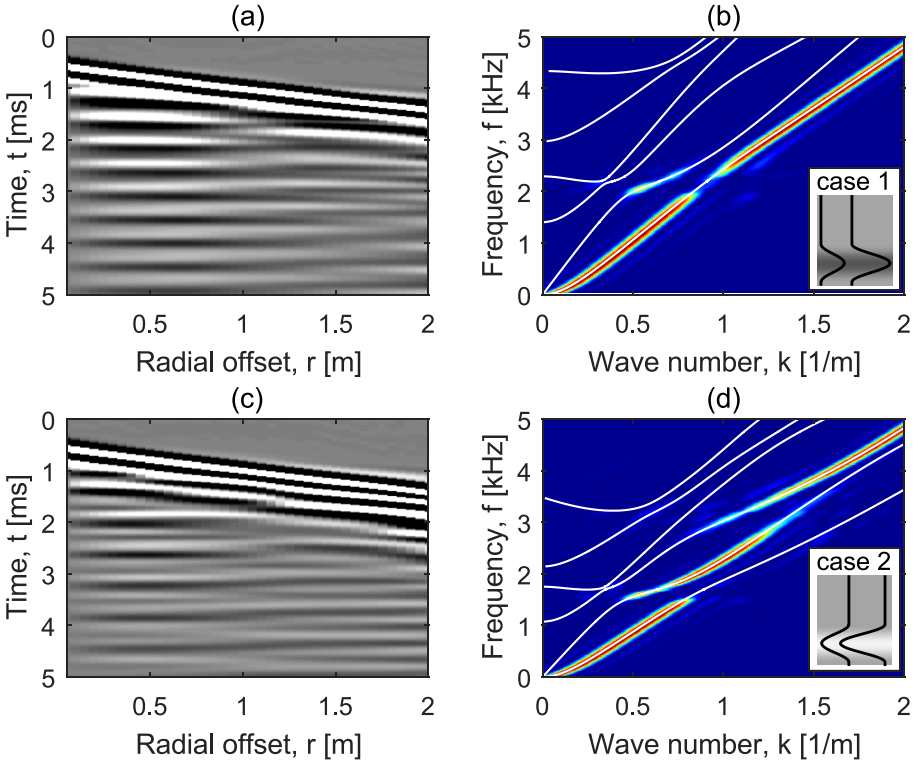

FIG. 7. (Color online) Data sets for (a) case 1 and (c) case 2. Estimation of wave number-frequency content for (b) case 1 and (d) case 2 and superimposed dispersion curves (solid lines) from SAFE analysis.

frequency content of the simulated response, a 2D discrete Fourier transform (DFT)[56] is performed with results for cases 1 and 2 displayed in Figs. 7(b) and 7(d), respectively. Here, it should be noted that the full range of the data sets is used to construct the DFT image; the full data set covers the time range 0–40 ms and radial range 0–10 m. In addition to the wave number-frequency estimation, the dispersion curves from the SAFE analysis in Sec. III are superimposed and shown in Figs. 7(b) and 7(d). For both cases, good agreement between the dispersion curves and the data set is observed; this result further verifies the correctness of the dispersion curves from the SAFE analysis. By comparing case 1 in Fig. 7(b) with case 2 in Fig. 7(d), a differentiation of surface wave mode at high frequency is observed: the surface wave is related to the M1 mode for case 1 and to the M3 mode for case 2. This result, due to the regions near the top and bottom surfaces being exposed to different mechanical properties, can also be observed by studying the mode excitability in Fig. 6. Naturally, in investigations of an unknown system, such behavior may—if not considered—lead to uncertainty and error in data evaluation.

To facilitate identification of the M4-ZGV mode frequency, the response signals within a radial distance of 1 m from the point source are summed.[29] As a result, the influence from the propagating modes is reduced, which is useful for improved detection of the ZGV frequency in practical testing. Note that other summation regions (radial distances) can be used as well; the radial distance may, for instance, be adjusted depending on plate thickness or anticipated ZGV wave length. A discrete Fourier transform of the summed signal is calculated and shown with absolute values in Fig. 8. For reference, the ZGV frequencies from the SAFE analysis are marked with vertical lines. Good agreement can be observed for all cases.

As predicted from the SAFE analysis, the M4-ZGV mode materializes as a resonance with high amplitude and distinct frequency, similar to the S1-ZGV Lamb mode. However, the acceleration amplitudes of the peaks differ slightly between the cases. This is related to at least two different effects. First, for a constant absolute displacement amplitude $|C|$ in frequency domain, the corresponding absolute acceleration amplitude is given by a quadratic parabola $|C|f^2$, see Fig. 8. This effect, which occurs because acceleration is given by a second temporal derivative of displacement, causes increased acceleration amplitudes at high frequencies and decreased amplitudes at low frequencies for a constant displacement amplitude in frequency domain. Second, the amplitude of the M4-ZGV mode shape is different between the top and bottom surfaces (Fig. 4). For case 1, the M4-ZGV mode has a vertical displacement amplitude at the top surface that is higher than that at the bottom surface, whereas the opposite holds for case 2. Nevertheless, it is concluded that the frequency of the peaks corresponding to the M4-ZGV mode is detected with the same robustness and accuracy as for the S1-ZGV Lamb mode in the studied nondestructive application. That is, a practical nondestructive evaluation using ZGV modes can be used even for cases 1 and 2. It is reasonable to assume that this result can be further extended and generalized to other inhomogeneous plates that are within the boundary limits or similar to cases 1 and 2. However, due to the increased complexity of the relation between mode frequency and material properties in inhomogeneous cases, the evaluation and interpretation of the observed frequency may be difficult. This emphasizes the need for a secondary and independent investigation to assess any potential influence from varying material properties.

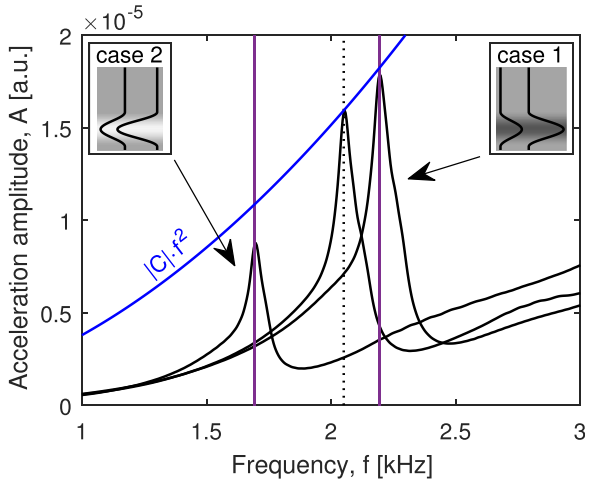

FIG. 8. (Color online) Discrete Fourier transform of summed acceleration response signals within 1 m distance from the impact source for case 1, case 2, and the isotropic reference case. Observed peaks correspond to the M4-ZGV mode (left and right peaks) and the S1-ZGV mode (middle peak). Vertical lines mark the ZGV frequencies from SAFE analysis. Parabola shows acceleration amplitude values corresponding to a constant absolute displacement amplitude $|C|$ at different frequencies.

V. CONCLUSION

Results from the SAFE analysis show that the M4 mode for both cases 1 and 2 exhibit a ZGV mode (M4-ZGV) that is similar to the S1 Lamb mode (S1-ZGV) for the isotropic reference case. Some differences in mode shape between M4-ZGV and S1-ZGV are observed, although it can be concluded that the overall characteristic of the M4-ZGV mode shape is common and similar to the S1-ZGV mode shape. No strict symmetric or antisymmetric modes exist for case 1 and case 2; however, one may loosely describe the M4-ZGV mode as approximately symmetric.

The SAFE analysis shows high mode excitability associated with the M4-ZGV mode. This is further verified in the simulation of a measurement application, as the M4-ZGV mode frequency is detected with the same accuracy and robustness as the S1-ZGV Lamb mode frequency. However, since a complex relation between mode frequency and material properties exists, the mode frequency cannot easily be translated to a representative mean value or other similarly established quantitative measure; thus, uncertainties or errors may arise in practical measurement applications.

A challenge with inhomogeneous material variation cases is the presence of a more complex wave field system. For cases 1 and 2, this can be observed, for instance, by the interchange of mode behavior, i.e., the so-called mode-kissing, as well as by the difference in the propagating surface wave mode at high frequency. For these cases, it is evident

that an assumption of homogeneous isotropy material (Lamb waves) is not feasible and cannot be considered as a robust mean value operator; an estimation using a Lamb wave model will not provide representative cross-sectional mean values for the plate in cases 1 and 2. Although this reasoning derives from a study of two synthetic cases, depending on the magnitude of the potential material variation, the same reasoning will hold for other inhomogeneous structures and applications as well.

To enable reliable evaluation procedures in practical nondestructive applications, results from this study highlight the general need for knowledge and understanding of the investigated system as well for assessment of the potential influence from varying material properties. The results also provide increased knowledge of ZGV modes and pave the way toward further improvements of nondestructive applications of plates, such as thick plate-like concrete structures in which material variations may occur.

ACKNOWLEDGMENTS

The Development Fund of the Swedish Construction Industry (SBUF, No. 13104) and The Swedish Radiation Safety Authority (SSM, No. SSM2017-956) are acknowledged for financial support of the study.

[1]C. Prada, D. Clorennec, and D. Royer, "Local vibration of an elastic plate and zero-group velocity Lamb modes," J. Acoust. Soc. Am. **124**(1), 203–212 (2008).
[2]E. Kausel, "Number and location of zero-group-velocity modes," J. Acoust. Soc. Am. **131**(5), 3601–3610 (2012).
[3]B. A. Auld, *Acoustic Fields and Waves in Solids, Vol. II*, 2nd ed. (Robert E. Krieger Publishing Company, Malabar, Florida, 1990).
[4]S. D. Holland and D. E. Chimenti, "Air-coupled acoustic imaging with zero-group-velocity Lamb modes," Appl. Phys. Lett. **83**(13), 2704–2706 (2003).
[5]I. Tolstoy and E. Usdin, "Wave propagation in elastic plates: Low and high mode dispersion," J. Acoust. Soc. Am. **29**(1), 37–42 (1957).
[6]C. Prada, O. Balogun, and T. W. Murray, "Laser-based ultrasonic generation and detection of zero-group velocity Lamb waves in thin plates," Appl. Phys. Lett. **87**(19), 194109 (2005).
[7]O. Baggens and N. Ryden, "Poisson's ratio from polarization of acoustic zero-group velocity Lamb mode," J. Acoust. Soc. Am. **138**(1), EL88–EL92 (2015).
[8]D. Clorennec, C. Prada, and D. Royer, "Local and noncontact measurements of bulk acoustic wave velocities in thin isotropic plates and shells using zero group velocity Lamb modes," J. Appl. Phys. **101**(3), 034908 (2007).
[9]C. Prada, D. Clorennec, T. W. Murray, and D. Royer, "Influence of the anisotropy on zero-group velocity Lamb modes," J. Acoust. Soc. Am. **126**(2), 620–625 (2009).
[10]M. Cès, D. Royer, and C. Prada, "Characterization of mechanical properties of a hollow cylinder with zero group velocity Lamb modes," J. Acoust. Soc. Am. **132**(1), 180–185 (2012).
[11]J. Laurent, D. Royer, T. Hussain, F. Ahmad, and C. Prada, "Laser induced zero-group velocity resonances in transversely isotropic cylinder," J. Acoust. Soc. Am. **137**(6), 3325–3334 (2015).
[12]S. Mezil, F. Bruno, S. Raetz, J. Laurent, D. Royer, and C. Prada, "Investigation of interfacial stiffnesses of a tri-layer using zero-group velocity Lamb modes," J. Acoust. Soc. Am. **138**(5), 3202–3209 (2015).
[13]S. Mezil, J. Laurent, D. Royer, and C. Prada, "Non contact probing of interfacial stiffnesses between two plates by zero-group velocity Lamb modes," Appl. Phys, Lett. **105**(2), 021605 (2014).
[14]M. Cès, D. Clorennec, D. Royer, and C. Prada, "Thin layer thickness measurements by zero group velocity Lamb mode resonances," Rev. Sci. Instrum. **82**(11), 114902 (2011).
[15]S. Raetz, J. Laurent, T. Dehoux, D. Royer, B. Audoin, and C. Prada, "Effect of refracted light distribution on the photoelastic generation of zero-group velocity Lamb modes in optically low-absorbing plates," J. Acoust. Soc. Am. **138**(6), 3522–3530 (2015).
[16]H. Bjurström and N. Ryden, "Detecting the thickness mode frequency in a concrete plate using backward wave propagation," J. Acoust. Soc. Am. **139**(2), 649–657 (2016).
[17]X. Dai, J. Zhu, Y.-T. Tsai, and M. R. Haberman, "Use of parabolic reflector to amplify in-air signals generated during impact-echo testing," J. Acoust. Soc. Am. **130**(4), EL167–EL172 (2011).
[18]J. Zhu and J. S. Popovics, "Imaging concrete structures using air-coupled impact-echo," J. Eng. Mechan. **133**(6), 628–640 (2007).
[19]B. Gérardin, J. Laurent, C. Prada, and A. Aubry, "Negative reflection of Lamb waves at a free edge: Tunable focusing and mimicking phase conjugation," J. Acoust. Soc. Am. **140**(1), 591–600 (2016).
[20]I. A. Veres, C. Grünsteidl, D. M. Stobbe, and T. W. Murray, "Broad-angle negative reflection and focusing of elastic waves from a plate edge," Phys. Rev. B **93**(17), 174304 (2016).
[21]F. Bruno, J. Laurent, P. Jehanno, D. Royer, and C. Prada, "Laser beam shaping for enhanced zero-group velocity Lamb modes generation," J. Acoust. Soc. Am. **140**(4), 2829–2838 (2016).
[22]F. Faëse, S. Raetz, N. Chigarev, C. Mechri, J. Blondeau, B. Campagne, V. E. Gusev, and V. Tournat, "Beam shaping to enhance zero group velocity Lamb mode generation in a composite plate and nondestructive testing application," NDT & E Int. **85**, 13–19 (2017).
[23]C. M. Grünsteidl, I. A. Veres, and T. W. Murray, "Experimental and numerical study of the excitability of zero group velocity Lamb waves by laser-ultrasound," J. Acoust. Soc. Am. **138**(1), 242–250 (2015).
[24]M. J. Sansalone and W. B. Streett, *Impact-echo: Non-destructive Evaluation of Concrete and Masonry* (Bullbrier Press, Ithaca, New York, 1997).
[25]A. Gibson and J. S. Popovics, "Lamb wave basis for impact-echo method analysis," J. Eng. Mech. **131**(4), 438–443 (2005).
[26]N. Ryden and C. B. Park, "A combined multichannel impact echo and surface wave analysis scheme for non-destructive thickness and stiffness evaluation of concrete slabs," *AS NT, 2006 NDE Conference on Civil Engineering* (2006), St. Louis, MO, pp. 247–253.
[27]R. Groschup and C. Grosse, "Mems microphone array sensor for air-coupled impact-echo," Sensors **15**(7), 14932–14945 (2015).
[28]R. Medina and M. Garrido, "Improving impact-echo method by using cross-spectral density," J. Sound Vib. **304**(3-5), 769–778 (2007).
[29]N. Ryden, "Enhanced impact echo frequency peak by time domain summation of signals with different source receiver spacing," Smart Struct. Syst. **17**(1), 59–72 (2016).
[30]M. S. Bouhdima, M. Zagrouba, and M. H. Ben Ghozlen, "The power series technique and detection of zero-group velocity Lamb waves in a functionally graded material plate," Can. J. Phys. **164**(2), 159–164 (2012).
[31]O. Abraham, B. Piwakowski, G. Villain, and O. Durand, "Non-contact, automated surface wave measurements for the mechanical characterisation of concrete," Constr. Build. Mater. **37**, 904–915 (2012).
[32]A. J. Boyd and C. C. Ferraro, "Effect of curing and deterioration on stress wave velocities in concrete," J. Mater. Civ. Eng. **April**, 153–158 (2005).
[33]J. S. Popovics, G. P. Cetrangolo, and N. D. Jackson, "Experimental investigation of impact-echo method for concrete slab thickness measurement," J. Kor. Soc. Nondestruct. Test. **26**(6), 427–439 (2006).
[34]J. S. Popovics, W. Song, J. D. Achenbach, J. H. Lee, and R. F. Andre, "One-sided stress wave velocity measurement in concrete," J. Eng. Mech. **124**(12), 1346–1353 (1998).
[35]S. Popovics, "Effects of uneven moisture distribution on the strength of and wave velocity in concrete," Ultrasonics **43**(6), 429–434 (2005).
[36]L. Qixian and J. H. Bungey, "Using compression wave ultrasonic transducers to measure the velocity of surface waves and hence determine dynamic modulus of elasticity for concrete," Constr. Build. Mater. **10**(4), 237–242 (1996).
[37]P. Turgut and O. F. Kucuk, "Comparative relationships of direct, indirect, and semi-direct ultrasonic pulse velocity measurements in concrete," Russ. J. Nondestr. Test. **42**(11), 745–751 (2006).
[38]A. M. Neville and J. J. Brooks, *Concrete Technology*, 2nd ed. (Prentice-Hall, Harlow, England), pp. 1–442 (2010).
[39]O. Baggens and N. Ryden, "Systematic errors in impact-echo thickness estimation due to near field effects," NDT & E Int. **69**, 16–27 (2015).
[40]O. Baggens and N. Ryden, "Near field effects and estimation of Poisson's ratio in impact-echo thickness testing," 41st Annu. Rev. Progr. Quantitative Nondestr. Eval. **1650**, 1415–1422 (2015).
[41]Alexander Gibson, "Advances in nondestructive testing of concrete pavements," Ph.D. thesis, University of Illinois, 2004.

[42]M. Cees, D. Clorennec, D. Royer, and C. Prada, "Edge resonance and zero group velocity Lamb modes in a free elastic plate," J. Acoust. Soc. Am. **130**(2), 689–694 (2011).
[43]H. Lamb, "On the flexure of an elastic plate," Proc. London Math. Soc. **s1-21**(1), 70–91 (1889).
[44]L. Rayleigh, "On the free vibrations of an infinite plate of homogeneous isotropic elastic matter," Proc. London Math. Soc. **20**(357), 225–234 (1889).
[45]M. J. S. Lowe, "Matrix techniques for modeling ultrasonic waves in multilayered media," IEEE Trans. Ultrason., Ferroelectr. Freq. Control **42**(4), 525–542 (1995).
[46]I. Bartoli, A. Marzani, F. L. di Scalea, and E. Viola, "Modeling wave propagation in damped waveguides of arbitrary cross-section," J. Sound Vib. **295**(3–5), 685–707 (2006).
[47]COMSOL Inc. Comsol multiphysics (r), 2016, URL http://www.comsol.-com (Date last viewed 2016-12-20).
[48]M. V. Predoi, M. Castaings, B. Hosten, and C. Bacon, "Wave propagation along transversely periodic structures," J. Acoust. Soc. Am. **121**, 1935–1944 (2007). ISSN 00014966.
[49]Q. Zhu and W. G. Mayer, "On the crossing points of Lamb wave velocity dispersion curves," J. Acoust. Soc. Am. **93**(4), 1893–1895 (1993).
[50]A. G. Every, "Intersections of the Lamb mode dispersion curves of free isotropic plates," J. Acoust. Soc. Am. **139**(4), 1793–1798 (2016).
[51]H. Uberall, B. Hosten, and M. Deschamps, "Repulsion of phase-velocity dispersion curves and the nature of plate vibrations," J. Acoust. Soc. Am. **96**(2), 908–917 (1994).
[52]M. Biot, "General theorems on the equivalence of group velocity and energy transport," Phys. Rev. **105**(4), 1129–1137 (1957).
[53]F. Treyssède and L. Laguerre, "Numerical and analytical calculation of modal excitability for elastic wave generation in lossy waveguides," J. Acoust. Soc. Am. **133**, 3827–3837 (2013).
[54]W. Ke, M. Castaings, and C. Bacon, "3d finite element simulations of an air-coupled ultrasonic NDT system," NDT & E Int. **42**(6), 524–533 (2009).
[55]M. Castaings, C. Bacon, B. Hosten, and M. V. Predoi, "Finite element predictions for the dynamic response of thermo-viscoelastic material structures," J. Acoust. Soc. Am. **115**(3), 1125–1133 (2004).
[56]C. B. Park, R. D. Miller, and J. Xia, "Multichannel analysis of surface waves," Geophysics **64**(3), 800–808 (1999).

Build version ☼2017-08-30 ◷13.12.45
(end of document)